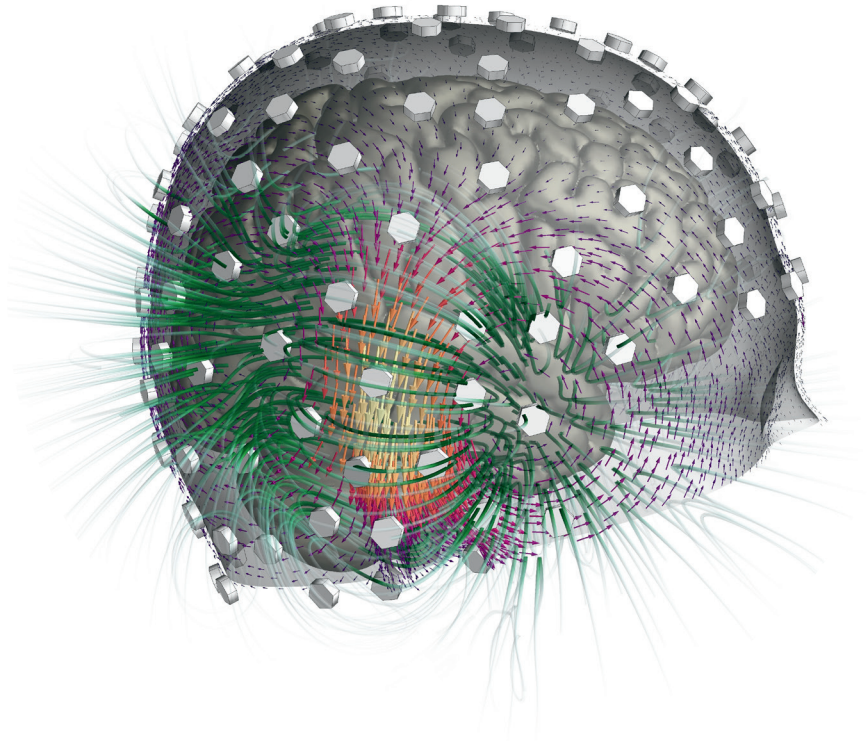


Development of an on-scalp MEG system using optically-pumped magnetometers

Rasmus Zetter



Development of an on-scalp MEG system using optically-pumped magnetometers

Rasmus Zetter

A doctoral dissertation completed for the degree of Doctor of Science (Technology) to be defended, with the permission of the Aalto University School of Science, at a public examination held at the lecture hall F239a of the school on the 15th of January 2020 at noon. The examination is publicly available via a remote connection, <https://aalto.zoom.us/j/69971504989>.

Aalto University
School of Science
Department of Neuroscience and Biomedical Engineering

Supervising professor

Prof. Lauri Parkkonen, Aalto University, Finland

Thesis advisor

Prof. Lauri Parkkonen, Aalto University, Finland

Preliminary examiners

Prof. Jens Haueisen, Technische Universität Ilmenau, Germany

Prof. Vittorio Pizzella, University of Chieti-Pescara, Italy

Opponent

Prof. Matthew Brookes, University of Nottingham, United Kingdom

Aalto University publication series

DOCTORAL DISSERTATIONS 222/2020

© 2020 Rasmus Zetter

ISBN 978-952-64-0213-0 (printed)

ISBN 978-952-64-0214-7 (pdf)

ISSN 1799-4934 (printed)

ISSN 1799-4942 (pdf)

<http://urn.fi/URN:ISBN:978-952-64-0214-7>

Unigrafia Oy

Helsinki 2020

Finland



Author

Rasmus Zetter

Name of the doctoral dissertation

Development of an on-scalp MEG system using optically-pumped magnetometers

Publisher School of Science

Unit Department of Neuroscience and Biomedical Engineering

Series Aalto University publication series DOCTORAL DISSERTATIONS 222/2020

Field of research Biomedical Engineering

Manuscript submitted 17 September 2020

Date of the defence 15 January 2021

Permission for public defence granted (date) 13 November 2020

Language English

☐ **Monograph**

☒ **Article dissertation**

☐ **Essay dissertation**

Abstract

Magnetoencephalography (MEG) is a noninvasive functional neuroimaging method in which the magnetic field due to the neuronal currents that constitute brain activity is measured using sensors outside the head. These *neuromagnetic* measurements can be used to make inference about brain function within neuroscientific research and clinical medicine.

Current state-of-the-art MEG systems utilize ultra-sensitive *superconducting quantum interference device* (SQUID) sensors that require cryogenic cooling and thermal insulation between the sensors and the subject's head. The thermal insulation necessitates a relatively large brain–sensor separation, leading to loss of signal as well as spatial resolution. Recent developments to another type of sensor, called *optically-pumped magnetometer* (OPM), has resulted in sensors with sufficient performance for MEG use. OPMs do not require cryogenic temperatures to operate and can thus be placed much closer to, or even directly in contact with the subject's scalp. Such *on-scalp* MEG systems will significantly improve signal amplitude as well as increase spatial resolution, and may thus enable the detection of phenomena so far only detectable in invasive measurements. In addition, the improved adaptability of OPMs will enable new types of MEG systems, including wearable MEG devices allowing for subject movement and smaller, low-cost systems.

This Thesis contributes to the development of an on-scalp MEG system based on OPMs and explores what such a system can or should consist of.

In particular, the requirements for how well the sensor positions must be known in order to estimate the MEG signal source within the brain are determined using simulations. Following the determination of these requirements, an optical method to localize the sensors that fulfills those requirements is developed and validated. Further, the performance of a first-generation on-scalp MEG system capable of source estimation is demonstrated and its performance compared to that of a state-of-the-art SQUID-based MEG system. Finally, a method and software package for magnetic field modeling and coil design is developed, which can be utilized for the next generation of on-scalp MEG systems.

Through these works, this Thesis provides a stepping stone for the continued development of on-scalp MEG as an imaging modality and demonstrates its future prospects.

Keywords magnetoencephalography, optically-pumped magnetometer, on scalp, neuroimaging, co-registration, stream function, coil design, magnetic field modeling, software

ISBN (printed) 978-952-64-0213-0

ISBN (pdf) 978-952-64-0214-7

ISSN (printed) 1799-4934

ISSN (pdf) 1799-4942

Location of publisher Helsinki

Location of printing Helsinki **Year** 2020

Pages 141

urn <http://urn.fi/URN:ISBN:978-952-64-0214-7>

Författare

Rasmus Zetter

Doktorsavhandlingens titel

Utveckling av ett magnetoencefalografi-system som använder optiskt pumpade magnetometrar

Utgivare Högskolan för teknikvetenskaper**Enhet** Institutionen för neurovetenskap och biomedicinsk teknik**Seriens namn** Aalto University publication series DOCTORAL DISSERTATIONS 222/2020**Forskningsområde** Medicinsk teknik**Inlämningsdatum för manuskript** 17.09.2020**Datum för disputation** 15.01.2021**Beviljande av disputationstillstånd (datum)** 13.11.2020**Språk** Engelska☐ **Monografi**☒ **Artikelavhandling**☐ **Essäavhandling****Sammandrag**

Magnetoencefalografi (MEG) är en noninvasiv metod för undersökning av hjärnfunktion i vilken det magnetfält som orsakas strömmar i hjärnans neuroner mäts med hjälp av sensorer runt om huvudet. Dessa *neuromagnetiska* mätningar används för att dra slutsatser gällande hjärnfunktion inom neurovetenskap och kliniskt bruk.

Nuvarande MEG-system använder mycket känsliga, supraledande sensorer som kräver kryogen nedkylning och värmeisolering mellan sensorerna och huvudet.

Värmeisoleringen kräver ett relativt stort avstånd mellan sensorerna och hjärnan, vilket leder till nedsatt känslighet och upplösning. Forsknings- och utvecklingsarbete inom de senaste två decennierna har lett till sensorer av en annan typ, så kallade *optiskt pumpade magnetometrar* (OPM), som har tillräckligt bra prestanda för att användas inom MEG. OPMs kräver inte kryogen nedkylning och kan därmed placeras mycket närmare eller rentav i direkt beröring med huvudet. Dessa så kallade *on-scalp* MEG-system har märkbart bättre känslighet och upplösning, och kan därmed möjliggöra mätning av signaler som hittills krävt invasiva mätningar. OPM-sensorernas anpassningsbarhet möjliggör dessutom nya typer av MEG-system, t.ex. "wearable" MEG i vilken försökspersonen kan röra sig fritt, samt mindre och förmånligare system.

Denna Avhandling bidrar till utvecklingen av ett on-scalp MEG-system som baserar sig på OPM-sensorer och utforskar vad ett sådant system kan eller bör bestå av. Mer specifikt, kraven på hur noggrant sensorernas positioner bör fastställas för att avgöra från vilken plats i hjärnan MEG-signaler härstammar avgörs med hjälp av simulationer. Efter att kraven fastställts utvecklas och valideras en optisk metod för att avgöra sensorernas position som uppfyller dessa krav. Därefter demonstreras ett första generationens on-scalp MEG-system baserat på OPM-sensorer och dess prestanda jämförs med ett SQUID-baserat MEG-system. Slutligen utvecklas en metod och mjukvarupaket för modellering av magnetfält och design av spolar som kan användas i utvecklingen av nästa generations MEG-system. I och med dessa insatser utgör denna Avhandling en språngbräda för fortsatt utveckling av on-scalp MEG som metod och demonstrerar dess framtida potential.

Nyckelord magnetoencefalografi, optiskt pumpad magnetometer, hjärnabbildning, spoldesign, modellering av magnetfält, mjukvara

ISBN (tryckt) 978-952-64-0213-0**ISBN (pdf)** 978-952-64-0214-7**ISSN (tryckt)** 1799-4934**ISSN (pdf)** 1799-4942**Utgivningsort** Helsingfors**Tryckort** Helsingfors**År** 2020**Sidantal** 141**urn** <http://urn.fi/URN:ISBN:978-952-64-0214-7>

Preface

The work described in this Thesis was performed at the Department of Neuroscience and Biomedical Engineering (NBE) at Aalto University School of Science. Magnetic resonance images were obtained at the Advanced Magnetic Imaging Centre and neuromagnetic measurements were carried out at the MEG Core facilities of Aalto Neuroimaging Infrastructure. Personal funding was provided by the Instrumentarium Science Foundation and the Swedish Cultural Foundation.

First and foremost, I would like to express my gratitude to my Thesis instructor and supervisor Prof. Lauri Parkkonen, who has been the best mentor I could imagine. I have always felt that I could rely on you for advice and guidance, regardless of the subject matter. Your breadth of knowledge and experience continues to impress me.

Research is a team effort, and I would like to thank all the co-authors of the publications included in this Thesis. From my co-authors, I would especially like to thank Dr. Joonas Iivanainen, who has been like a ‘brother in arms’ during our time together at NBE, and the vast majority of my work has in some effect been performed together with you. It has been great to simply be able to spin my chair around in order to bounce some ideas in our shared office. I would also like to thank Dr. Antti Mäkinen, who is an immensely capable scientist. After some years of working on different projects with similar challenges, a number of brainstorming sessions with Antti and Joonas lead to a fruitful collaboration of which I am very proud. Further, I would also like to thank Docent Matti Stenroos, whose excellent advice and patient teaching has greatly improved my physics knowledge and intuition as well as sharpened my critical thinking skills both in science and in my daily life.

I would like to thank the pre-examiners of this Thesis, Prof. Jens Haueisen and Prof. Vittorio Pizzella, for their thoughtful evaluation of and feedback on the manuscript of this Thesis. I would also like to thank Dr. Christoph Pfeiffer, Dr. Joonas Iivanainen and Prof. Lauri Parkkonen for reading through the manuscript of this Thesis and offering their feedback and critique. Your input was a huge relief and greatly appreciated.

I would like to thank my fellow members of the neuroimaging methods (NIMEG) research group, including my former office-mates Ivan Zubarev and

Dovile Kurmanaviciute, Dr. Christoph Pfeiffer, Dr. Linda Henriksson and Dr. Narayan Subramaniyam as well as our research assistants Mikael Grön, Markus Henttonen, Karoliina Hakkarainen, Elias Lius and Santeri Simanainen. I would especially like to thank Ivan Zubarev for the collaboration, which while not included in this thesis, was an incredible learning experience for and taught me most of what I know about machine learning.

NBE has a good community, with good conversation and inspirational scientific discourse taking place at typical group lunches and coffee breaks. I'd like to thank all my colleagues at NBE for the friendship and camaraderie over the years, including Dr. Tuomas Mutanen, Marko Havu, Dr. Niko Mäkelä, Dr. Lari Koponen, Iiro Lehto, Koos Zevenhoven, Dr. Victor Souza, Mikko Nyrhinen, Aino Tervo, Pauliina Hirvi and many more for creating such a warm 'NBE spirit'.

I would also like to thank Prof. Synnöve Carlson who originally took me on as a research assistant during my time as an undergraduate. I developed greatly as a budding scientist under your guidance. In this position, I also had the pleasure to work with Dr. Juha Gogulski, who truly made me feel like an equal part of the team.

I would also like to thank my family and especially my parents Monica and Bertil, who have always been supportive of and interested in my studies and work. My warmest thanks to all my friends, who bring some much-needed balance to my otherwise research-dominated life, whether it is by accompanying me on hikes over mountains or board game nights inside. Lastly, thanks to Johanna for all your love, support, and patience.

Esbo, December 7, 2020,

Rasmus Zetter

Contents

Preface	1
Contents	3
List of Publications	5
Author's Contribution	7
Abbreviations	9
1. Introduction	11
2. Aims of the Thesis	13
3. Background	15
3.1 Magnetoencephalography (MEG)	15
3.1.1 The neural sources	15
3.1.2 Signal characteristics	17
3.2 MEG Instrumentation	18
3.2.1 Sensor arrays and sampling	18
3.2.2 Shielding and interference rejection	19
3.3 Source modeling in MEG and EEG	21
3.3.1 The forward problem	22
3.3.2 The inverse problem	24
3.3.3 Co-registration	27
3.4 Optically-pumped magnetometers (OPMs)	29
3.4.1 Physical principle of operation	29
3.4.2 Sensor components	35
3.4.3 OPM-based MEG	36
3.5 Magnetic field modeling using stream functions	36
3.5.1 Computations using the discrete stream function	37
3.5.2 Stream-function optimization and coil design	40
3.5.3 Equivalent surface current models	44

4. Summary of Publications	47
4.1 Publication I: Requirements for Coregistration Accuracy in On-Scalp MEG	47
4.2 Publication II: Optical co-registration of MRI and on-scalp MEG	48
4.3 Publication III: Potential of on-scalp MEG: Robust detection of human visual gamma-band responses	49
4.4 Publication IV: Magnetic-field modeling with surface currents Part II: Implementation and usage of bfieldtools	51
5. Discussion	53
5.1 OPM-MEG system design	53
5.1.1 OPM sensor design	53
5.1.2 Shielding	54
5.1.3 Wearable MEG	55
5.1.4 Co-registration	55
5.1.5 Sampling	56
5.2 Coil design & stream functions	57
5.2.1 Active shielding	57
5.2.2 OPM design	57
5.3 Prospects of on-scalp MEG	58
References	59
Publications	75

List of Publications

This thesis consists of an overview and of the following publications which are referred to in the text by their Roman numerals.

I Rasmus Zetter, Joonas Iivanainen, Matti Stenroos and Lauri Parkkonen. Requirements for Coregistration Accuracy in On-Scalp MEG. *Brain Topography*, 31:931–948, June 2018.

II Rasmus Zetter, Joonas Iivanainen and Lauri Parkkonen. Optical Co-registration of MRI and on-scalp MEG. *Scientific Reports*, 9:5490, April 2019.

III Joonas Iivanainen*, Rasmus Zetter* and Lauri Parkkonen. Potential of on-scalp MEG: Robust detection of human visual gamma-band responses. *Human Brain Mapping*, 41:150–161, September 2019.

IV Rasmus Zetter, Antti J Mäkinen, Joonas Iivanainen, Koos C J Zevenhoven, Risto J Ilmoniemi and Lauri Parkkonen. Magnetic field modeling with surface currents. Part II. Implementation and usage of bfieldtools. *Journal of Applied Physics*, 128:063905, August 2020.

*These authors contributed equally to this work.

Author's Contribution

Publication I: “Requirements for Coregistration Accuracy in On-Scalp MEG”

The Thesis author planned the study with LP and the simulations together with all co-authors. The Thesis author performed the simulations using field modeling tools provided by MS. He analyzed the results and wrote the manuscript with support and input from all co-authors.

Publication II: “Optical Co-registration of MRI and on-scalp MEG”

The Thesis author developed the presented co-registration method. He designed and performed the simulations with design input from JI and LP. The Thesis author performed the empirical experiment with assistance from JI. He was the principal writer of the manuscript, with JI and LP commenting on the text.

Publication III: “Potential of on-scalp MEG: Robust detection of human visual gamma-band responses”

The Thesis author and JI contributed equally to this study. The Thesis author performed the measurements and analyzed the data together with JI. He also developed the data analysis methods with JI. The Thesis author wrote the article together with JI with support and supervision by LP.

Publication IV: “Magnetic field modeling with surface currents. Part II. Implementation and usage of bfieldtools”

The Thesis author co-created the software described in the article together with AJM and JI. The application examples in manuscript were conceived by the Thesis author, JI and AJM in the context of needs and ideas that had been discussed with KCJZ, RJI and LP within projects where neuroimaging technologies are being developed. The Thesis author wrote the article with input from all co-authors.

Abbreviations

BCI	brain-computer interface
BEM	boundary-element method
BSS	blind source separation
DICS	dynamic imaging of coherent sources
ECD	equivalent current dipole
EEG	electroencephalography
FEM	finite-element method
FID	free-induction decay
HPI	head position indicator
ICA	independent component analysis
ICP	iterative closest point
LCMV	linearly constrained minimum-variance
MEG	magnetoencephalography
MNE	minimum-norm estimate
MR	magnetic resonance
MRI	magnetic resonance imaging
MSR	magnetically shielded room
OPM	optically-pumped magnetometer
PCB	printed circuit board
PSP	postsynaptic potential

Abbreviations

RE	relative error
SD	spin destruction
SE	spin-exchange
SEF	somatosensory evoked field
SERF	spin-exchange relaxation-free
SFT	superconducting flux transformer
SLAM	synchronous light-pulse atomic magnetometer
SNR	signal-to-noise ratio
SQUID	superconducting quantum interference device
SSP	signal-space projection
SSS	signal-space separation
TBI	traumatic brain injury
TMS	transcranial magnetic stimulation
VCSEL	vertical-cavity surface-emitting laser

1. Introduction

The brain, as an organ, is the embodiment of who we are. It holds within the secrets of humanity, the mechanisms that enable our cognition and consciousness. A system capable of these remarkable feats must undeniably also be remarkably complex. Indeed, an adult human brain contains ~ 100 billion (10^{11}) neurons with ~ 100 trillion (10^{14}) inter-neuron connections [1, 2], and even a single neuron can perform complicated mathematical operations [3]. In order to even scratch the surface of ‘understanding the brain’, we need to measure brain function at scales ranging from single-cell measurements to macroscopic recordings of the entire brain. In the latter case, it is preferable to perform these recordings noninvasively as we tend to dislike opening up the skulls of our fellow man.

There are several noninvasive methods to indirectly measure brain function on the macroscopic scale through the metabolism or hemodynamics of cortical tissue, but the indirect nature of these methods means that they cannot resolve brain activity at the millisecond-timescale of the brain. In electroencephalography (EEG), brain activity is directly measured by recording the electric potential distribution on the scalp. EEG can resolve brain activity on a sub-millisecond scale but lacks spatial detail due to the potential being “blurred” by volume conduction in the various tissues of the head [4]. Magnetoencephalography (MEG), as suggested by the name, functions by measuring the magnetic field produced by the brain using sensors around the head [5]. MEG is also a direct measure of brain activity and has the same high temporal resolution as EEG, but has higher spatial resolution as the magnetic field is not affected by volume conduction to the same extent as the electric potential [5].

MEG has been an important tool in studying the fast dynamics of the brain in neuroscientific research and clinical medicine during the last few decades. Areas of study include attention, motor and language function, as well as consciousness (for a review see, e.g., [6, 7]). In clinical use, MEG is mainly applied in pharmacoresistant epilepsy cases [8] and the preoperative mapping of eloquent cortical areas [9], e.g. for the removal of brain tumors [10]. Detection of (mild) traumatic brain injury (TBI) appears to be a promising new clinical application for MEG [11, 12].

Since the neuromagnetic fields measured by MEG are very weak — on the

scale of a billionth of the Earth’s geomagnetic field — exceptionally sensitive equipment is needed for MEG. In addition, one needs to attenuate environmental magnetic noise considerably. Therefore, measurements are carried out in magnetically shielded rooms (MSRs) and sophisticated signal processing techniques are used to minimize noise.

To this point, the main type of magnetometer used for MEG has been the superconducting quantum interference device (SQUID). These sensors require cryogenic temperatures in order to function, and liquid helium is used to cool them to ~ 4 K (-269° C). The SQUID sensors are thus placed within a helmet-shaped insulated container, a *dewar*. Due to this insulation the SQUIDs are placed at least ~ 2 cm from the scalp. As sensitivity and spatial resolution are directly related to the distance between the brain and the sensors this results in significant signal degradation. In addition, the position of the sensors cannot be adapted to conform to the head shape of individual subjects, which can further increase the sensor–scalp separation and weaken sensitivity.

Within the last 10–15 years optically-pumped magnetometers (OPMs) [13] with high enough sensitivity to be used for MEG have been developed. The major advantage of this type of sensor is that it does not require cryogenic cooling and can thus be placed much closer to the scalp, boosting the sensitivity to neuromagnetic sources considerably and improving spatial resolution. These improvements may enable the detection of phenomena that thus far are only detectable in invasive measurements. Such *on-scalp* MEG systems introduce several unknowns and practical challenges, some of which are addressed by this Thesis.

In the next Section, the specific aims of this Thesis are listed, after which the basics of MEG signal generation and the characteristics of the signal measured by MEG are reviewed. The following section (3.2) gives an overview of current MEG instrumentation. Thereafter, the topic of the Thesis shifts to describe the OPMs that are now applied for on-scalp MEG and to describe a magnetic field modeling framework that can be used in MEG. The studies included in this Thesis are briefly outlined in Section 4, after which the summary part of the Thesis is concluded with a forward-looking discussion of the Thesis topic in Section 5.

2. Aims of the Thesis

The main goals of this Thesis were to contribute to the development of a practical, usable on-scalp MEG system, as well as to explore what such a system can or should consist of.

In Publication I, we set out to find out how precisely one must know where the on-scalp sensors are in relation to the brain in order to achieve good source modeling performance, and in specifically what ways co-registration error affects source modeling performance.

Knowing the requirements of co-registration accuracy for on-scalp MEG, in Publication II we developed a co-registration method for our on-scalp MEG system that fulfills these requirements. Additionally, we aimed to make the co-registration method fast, easy to use and generally practical.

Having a source modeling-capable first-generation OPM-based on-scalp MEG system, we set out to apply it to a neuroscientific application. In Publication III we demonstrate its performance in a visual-gamma task and compare it to a state-of-the-art SQUID-based MEG system.

OPMs and MEG instrumentation in general require coils used for magnetic shielding and negative feedback. In order to design coils for future OPM sensors and MEG systems, in Publication IV we developed a software package for magnetic field modeling and coil design. This software package is of use both to us and others when designing the next-generation OPM-based MEG systems, as well as in other applications.

3. Background

3.1 Magnetoencephalography (MEG)

3.1.1 The neural sources

To understand the signal measured by MEG, one must first look at the brain on the level of cellular biophysics. The human brain consists of *neurons* that perform information processing, as well as supporting cells called *glia* that provide a variety of essential functions such as vasodilation, enforcement of ion balance, and transport of nutrients. The cell bodies of neurons are concentrated on the surface of the brain or *cortex*, called *gray matter*. The interior of the brain is mainly occupied by nerve fibers; this is called *white matter* due to its characteristic appearance.

As seen in Fig. 3.1, neurons consist of a cell body or *soma*, a tree of *dendrites* that receive input from other neurons and an *axon*, which conveys the output of the neuron to other neurons. The end of the axon and a dendrite of another neuron form a synapse, where signaling is performed chemically using substances called *neurotransmitters*.

Within the cell membrane lie *ion pumps*, which as the name implies actively move certain ion species across the membrane. Using these pumps, a transmembrane resting state potential of approximately -70 mV (the inside of the cell is more negative than the extracellular fluid) is maintained by pumping potassium and sodium ions across the membrane.

When neurotransmitters arrive at the cell membrane of the receiving neuron in a synapse, i.e. at the post-synaptic membrane, *ion channels* in the membrane are opened, selectively letting specific ion species move passively through. Depending on the type of neurotransmitter, different ion channels will open, either raising the transmembrane potential and thus causing an excitatory *post-synaptic potential* (PSP) or lowering the potential and causing an inhibitory PSP. Regardless of transmembrane potential, there is no accumulation of charge



Figure 3.1. Illustration of a stereotypical pyramidal neuron.

within the cell, and thus when there is inwards or outwards flow of ions at a synapse, be they positive or negative, there are compensating *volume ion currents* elsewhere along the cell membrane that close the ion current loop.

PSPs are relatively long-lasting (on the order of a few milliseconds to hundreds of milliseconds), and the PSPs from all inputs to the cell are nonlinearly summated [3]. If the resultant transmembrane potential at the root of the axon by the soma, i.e. at the *axon hillock*, exceeds an activation threshold of approximately -55 mV, an *action potential* is generated. An action potential consists of a rapid change of membrane voltage due to a sudden influx of sodium ions such that the potential suddenly jumps to $+35$ mV. The potential returns to the resting state in 1–2 milliseconds due to potassium ions flowing out through the membrane. This repolarization is followed by a refractory period of 1 millisecond. The action potential is actively propagated along the axon to the synapse without decaying in amplitude, where neurotransmitters are released in response. A large part of neurons in the central nervous system have a *myelin sheath*, an electrically insulating layer, covering their axons. This feature greatly accelerates the propagation of action potentials and lessens the overall energy use of the nervous system.

Intracellular potential changes due to PSPs cause a current flow along the dendrites that can be modeled as a current dipole, leading to a dipolar magnetic field that decays roughly by $1/r^2$. The current pattern of action potentials can be modeled as two oppositely directed current dipoles traveling along the axon, producing a quadrupolar magnetic field that decays by $1/r^3$ [5]. The magnetic field measured by MEG primarily originates in a type of neuron in the gray matter of the brain called *pyramidal neurons*. These neurons can give rise to extracranial magnetic fields since their apical dendrites are all oriented perpendicularly to the surface of the cortex. Thus, the magnetic fields of nearby neurons are spatially summated. As PSPs have a relatively long lifetime, significant temporal summation of the PSPs of neighboring neurons

also occurs. Since action potentials are much more short-lived and their magnetic field disappears at shorter distances, the vast majority of the magnetic field measured by MEG stems from synchronous PSPs from tens of thousands of neurons [14].

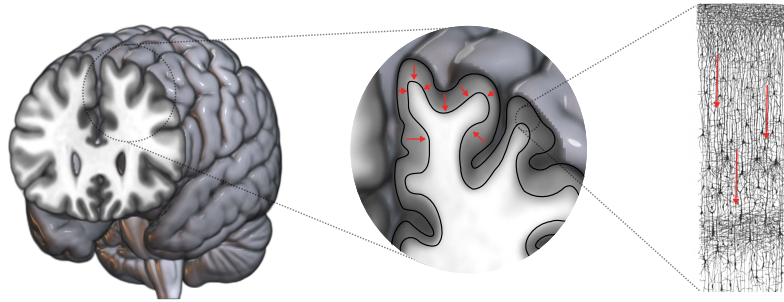


Figure 3.2. The main source of MEG signals is synchronous postsynaptic currents in the apical dendrites of pyramidal neurons (seen as red arrows in the middle and right-side panels). The right-side panel is based on a drawing by Ramón y Cajal in 1889 [15].

Besides temporal and spatial summation, several other factors affect the measured signal strength. As mentioned, signal strength is reduced as the spatial sensor–source separation grows. Another factor that affects the signal strength is source orientation. Due to the folded surface of the human brain (Fig. 3.2, left panel) the orientation of pyramidal cells varies significantly. At the most superficial parts of the cortex, the *gyral crowns*, the pyramidal cells are oriented radially with respect to the head, while at the *gyral walls* they are oriented tangentially. Due to the geometry of the head, MEG is mostly sensitive to tangential sources and insensitive to radial sources [5], and thus the majority of signal comes from the gyral walls (Fig. 3.2, middle panel). Considering the loss of signal along depth, the sources to which MEG is most sensitive are at the superficial edges of the *sulci* (i.e. the grooves in the surface of the cortex).

3.1.2 Signal characteristics

The neuromagnetic signal typically measured with MEG spans a frequency range of ~ 0.5 –1000 Hz [7]. The MEG frequency spectrum generally follows a $1/f$ relation, with most of the signal power residing in the low frequencies (< 80 Hz). The MEG signal spectrum is loosely divided into a number of frequency bands, whose definitions are partially based on historical reasons and partially on neurophysiology [16]. The most typical division is delta (1–4 Hz), theta (4–8 Hz), alpha (8–12 Hz), beta (12–30 Hz), low gamma (30–60 Hz), high gamma (60–250 Hz) and fast ripples (200–400 Hz), although the definitions used in the literature vary widely [17]. At > 500 Hz weak activity, thought to be due to axonal activity (i.e. action potentials), can be detected [18].

Within these frequency bands there are ongoing, periodic signals, often termed

oscillations or rhythms, that are deemed characteristic for each band. Examples of these include the occipital alpha rhythm, the Rolandic μ -rhythm and somatomotor beta rhythm (for a review and discussion, see e.g., [19]) as well as occipital narrowband gamma oscillations [20]. The rhythms are theorized to have different roles in cognition [21, 22, 23, 24], e.g. modulating top-down (from higher cognitive functions to lower-level sensory cortices) and bottom-up cortical networks or governing attention.

While the general idea of different frequency bands having different roles is useful, the specific delineation of bands used is a historical artifact both in terms of the frequencies chosen and the implied sinusoidal basis; much of the literature surrounding brain oscillations have (implicitly) assumed that the brain works using sinusoidal signals. This has recently been shown not to be the case for several of these rhythms [25], with some of them having clear nonsinusoidal components.

In addition to these structured signals and rhythms, there is also “noise-like” $1/f$ activity that is especially visible in the high gamma frequency band due to the absence of other prominent signals [26, 27]. This has been termed broadband gamma, and it is thought to reflect the local population firing rate of the brain [28, 29, 30, 31]. While broadband gamma can be seen in some noninvasive MEG measurements, it is much more prevalent in invasive recordings [32, 33, 34].

The spatial structure of the MEG signal is similar to most physical systems in the sense that the spatial coherence of signals generally decreases with increasing frequency. Focal sources, involving only some square millimeters of cortex firing, result in simple dipolar field patterns. When several cortical regions are active, the measured magnetic field is a superposition of several of these field patterns. As activity from cortical networks spanning the whole cortex can be measured (e.g. [35]), the spatiotemporal pattern of MEG signals is very complex. In practice, the measured signal amplitudes are at the scale of femto- to picoteslas, and thus MEG requires very sensitive magnetometers.

3.2 MEG Instrumentation

3.2.1 Sensor arrays and sampling

The first human MEG measurements were performed using a conventional induction coil magnetometer by Cohen in 1968 [36]. In this first experiment the occipital alpha rhythm could be seen after extensive averaging of data. Around the same time, the first SQUID was developed [37] and soon after the first MEG measurements using this new technology were performed [38]. Ever since, the SQUID has been more or less the only sensor type used for MEG and has until recently been unchallenged as the most sensitive type of magnetometer developed. Current state-of-the-art MEG systems comprise hundreds of SQUID

sensors in a uniformly spaced sensor array covering the whole head.

SQUIDs are typically very small to minimize flux noise. To improve their field sensitivity, *superconducting flux transformers* (SFTs) are used. An SFT consists of a large *pick-up coil* positioned as close to the brain as possible and smaller *signal coil* located directly on top the SQUID. These two coils are connected in series, thus “concentrating” the flux from the large pick-up coil into the SQUID through the signal coil. By using different shapes for the pick-up coil, the sensitivity profile of SQUIDs can easily be manipulated: a magnetometer is constructed using a single loop for the pick-up coil, first-order gradiometers are constructed using two oppositely-wound loops, and so forth. Gradiometers measure the gradient of the magnetic field, and thus they inherently reject common-mode signals such as fields from far-away sources.

As both SQUIDs and SFTs need to be superconducting to function they are immersed in liquid helium, which has a boiling temperature of 4.2 K. Both the sensors and the helium are housed within a large insulating helmet-shaped *dewar*. The dewar should be as thin as possible to bring the pick-up coils as close to the head as possible, and on the other hand it needs to be insulating enough to keep helium boil-off rate at acceptable levels.

In typical SQUID-MEG systems, the dewar limits the sensor–scalp distance to > 2 cm. In emerging on-scalp MEG systems, the sensors can be placed within millimeters of the scalp (see Fig. 3.3), significantly boosting sensitivity. Since higher spatial frequencies decay at smaller distances, the dewar also limits the spatial resolution of MEG measurements. According to recent simulations [39], the maximum number of spatial degrees of freedom in any neuromagnetic field measured by on-scalp MEG and SQUID-MEG is approximately 300 and 100, respectively. This number can be interpreted as the number of sensors in a uniformly spaced sensor array needed to reconstruct the measured field in noise-less conditions. These numbers roughly correspond to the “rule of thumb” according to which the sensor spacing needed to adequately sample the neuromagnetic field should be approximately the same as the sensor–cortex distance [40].

3.2.2 Shielding and interference rejection

Passive shielding

Regardless of the type of sensor used to measure MEG, the most important means to avoid environmental interference that would drown out the MEG signal or even prevent the sensors from reaching their operating range is to employ a *magnetically shielded room* (MSR). The passive shielding provided by an MSR comes down to two different factors. For shielding at low frequencies, high-permeability material is used to provide a low-reluctance path for the interfering magnetic field along the walls of the MSR, thus reducing the field within the room. To this end, a nickel-iron alloy (called μ -metal) with a relative

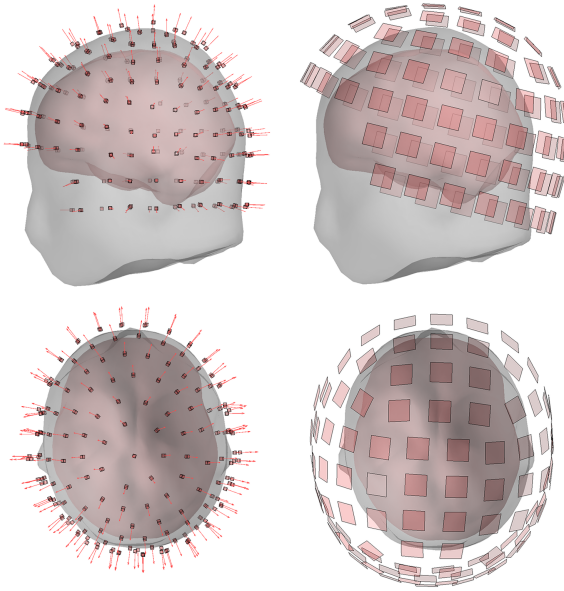


Figure 3.3. Whole-head OPM-based on-scalp MEG (left, 184 sensors) and SQUID-MEG (right, 102 sensor locations) sensor arrays, showing the OPM sensitive volumes and SQUID pick-up coils both from the side (upper row) and top-down (lower row). The arrows represent the sensitive axis of the OPMs.

permeability of > 50000 is commonly employed. Second, to shield against higher frequencies (> 10 Hz) eddy-current shielding is used in the form of a high-conductivity material, usually aluminum or copper [41, 42]. Practical shielded rooms employ several layers of shielding of both types in the walls to improve the total shielding factor. These *multi-layer* MSRs can weigh up to tens of tons and thus MEG systems are usually located on bottom floors or in basements where structural support can be built to withstand the load. Additionally, as μ -metal is quite costly and a large amount of it is used in multi-layer MSRs, the expense of the MSR constitutes a large part of the investment for a new MEG system.

Due the aforementioned limitations imposed by large and heavy MSRs, there is a recent trend towards lighter and smaller *person-sized shields*. These can, e.g., be cylinder-shaped [43] or in a “phone-booth” form factor. There are no inherent reasons as to why a person-sized shield could not be used with SQUID-based MEG systems, but most of these smaller shields are in use with OPM-based MEG systems [43, 44].

Active shielding

Passive magnetic shielding can be enhanced by adding active shielding systems that work in a feedforward mode or in a negative feedback loop by applying a magnetic field that cancels the measured field using a set of coils wrapped around or inside the shield. When using active shielding, less extensive passive

shielding can suffice [45, 46]. Many lighter MSR and person-sized shield designs rely on active shielding to achieve sufficient performance. Still, active shielding is no panacea, and presents a number of technical problems on its own [47].

The sensor array itself and the pick-up coils also have an effect on interference levels. For example, gradiometers provide inherent suppression of interference from faraway sources, since both coils will experience the same magnetic field and as they are oppositely wound it is canceled out. In the case of magnetometers, one or several reference sensors placed at a small distance from the sensor array can be used for the same effect by subtracting the measured reference signal, in effect creating a synthetic gradiometer [5].

Software-based interference rejection

In addition to hardware-based interference rejection methods, several software-based methods based on signal processing or different kinds of physical modeling of the measurement are also used. In signal-space projection (SSP) [48], a representative “interference vector” is determined from the most significant principal components of empty-room or resting-state data, whereafter this vector is projected out of the measurement data. In signal-space separation (SSS) [49, 50], the measurement signal is fitted to a spherical-harmonics model of the magnetic field. In this representation the signal is divided into two harmonic series, one of which originates from within a spherical volume inside the sensor array and the other originates from outside the sensor array. The interference originating from outside the sensor array can then simply be removed from the model, after which the data are transformed back into the signal space. Finally, blind source separation (BSS) techniques based solely on the statistical properties of the data, such as independent component analysis (ICA) [51], are also widely used in order to reject interference, often in conjunction with SSP and SSS.

3.3 Source modeling in MEG and EEG

In clinical practice and in neuroscientific research, one uses MEG signals to perform inference on brain function and pathologies. In clear-cut cases, simply interpreting the signals as measured by the sensor array is sufficient. Often, one wants to determine from where in the brain some MEG signal originated in order to do more exact inference. In practice, this means using the magnetic field measured at the sensor locations to infer the current sources within the volume conductor that is the head. Unfortunately, this problem is ill-posed as there can be an infinite number of current source distributions within the head that result in any single measured magnetic field distribution outside the head. In order to make this so-called *inverse problem* well-posed, one must constrain the problem by adding prior information. In MEG, some current distributions are more physiologically likely than others, and thus we have a number of different

priors, leading to different solutions.

3.3.1 The forward problem

In order to infer the neural current sources in MEG, one must first construct a *forward model* describing how these current sources map to the MEG measurements. In practice, the primary source current distribution is discretized onto a *source space* composed of a set number M of source points. This source space may be *cortically constrained*, meaning that all source points are on the cortical surface, or *volumetric* meaning that it covers both white and gray matter in a grid-like manner. Cortically constrained source spaces can further constrain the source orientation to be normal to the cortical surface, while volumetric source spaces typically consist of three orthogonal sources at each location.

Considering the source vector $\mathbf{x} \in \mathbb{R}^{M \times 1}$, where each element corresponds one of M primary current sources within the brain, the measured MEG signal $\mathbf{y} \in \mathbb{R}^{N \times 1}$ (each element corresponding to one of N sensors) at a single time instant is given by the linear mapping

$$\mathbf{y} = \mathbf{G}\mathbf{x} + \mathbf{n}. \quad (3.1)$$

Here, the mapping operator $\mathbf{G} \in \mathbb{R}^{N \times M}$ determines how any primary source current is seen by the sensors, and \mathbf{n} is additive (sensor) noise not modeled by the linear relationship. \mathbf{G} is often termed the lead-field matrix, gain matrix or forward operator in MEG and EEG literature. Each column of \mathbf{G} represents the topography of a source (i.e., how the source couples to each of the sensors), while each row represents the sensitivity of a sensor to all sources (the so-called lead field of that sensor).

Starting from the quasi-static approximation of Maxwell's equations, one can compute \mathbf{G} using a model of the head volume conductor. In practice, the gain matrix is determined numerically using the *boundary element method* (BEM) [52], or the *finite element method* (FEM) [53]. To apply the BEM, the head is modeled as a piece-wise homogeneous volume conductor with K boundary surfaces separating regions of different conductivities (Fig. 3.4, left). In the FEM, the head is instead divided into a larger number of volumetric mesh elements, each of which can have a unique conductivity (Fig. 3.4, right). If the conductivity or geometry of live tissue is not known to high spatial detail, the main advantage of FEM does not apply. Thus, the BEM is more commonly used in experimental MEG.

On a macroscopic scale, the total neural current distribution $\vec{J}_{\text{tot}}(\vec{r}) = \vec{J}_p(\vec{r}) + \vec{J}_v(\vec{r})$ can be divided into two parts: the primary current \vec{J}_p corresponding to the macroscopic current dipole model, and the volume return current \vec{J}_v inside the head volume conductor. To obtain the magnetic field $\vec{B}(\vec{r})$ produced by $\vec{J}_{\text{tot}}(\vec{r})$ for the piece-wise homogeneous model used in BEM, one applies the *Geselowitz*

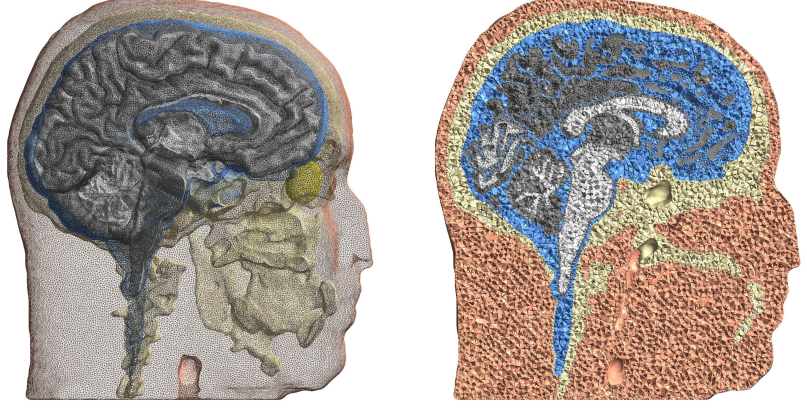


Figure 3.4. Left: Example of BEM boundary meshes using realistic surfaces reconstructed from MRI. Right: Alternatively, volumetric meshes are used when applying the FEM. Both figures show a cut-through from the midline, with the color-coding indicating tissues with different conductivity. Figure generated using SIMNIBS example data [54].

formula [55]:

$$\vec{B}(\vec{r}) = \vec{B}_0(\vec{r}) + \frac{\mu_0}{4\pi} \sum_{k=1}^K (\sigma_k^+ - \sigma_k^-) \int_{S_k} \phi(\vec{r}') \frac{(\vec{r} - \vec{r}')}{\|\vec{r} - \vec{r}'\|^3} \times d\vec{S}_k, \quad (3.2)$$

where σ_k^+ and σ_k^- correspond to the conductivities in the regions on the outer and inner side of the k th boundary, S_k is the surface of the k th boundary, the integration element dS_k is normal to that surface and μ_0 is the permeability of free space. The first term

$$\vec{B}_0(\vec{r}) = \frac{\mu_0}{4\pi} \int_{V'} \frac{\vec{J}_p(\vec{r}') \times (\vec{r} - \vec{r}')}{\|\vec{r} - \vec{r}'\|^3} dV' \quad (3.3)$$

is the contribution of the primary current \vec{J}_p and the second term in Eq. 3.2 is due to the volume current \vec{J}_v . Eq. 3.2 holds for all locations \vec{r} not on the surfaces S_k . It is evident that the absolute conductivity of the different regions does not matter, only the difference across boundaries. Even more importantly, the potential ϕ only has to be calculated at the boundaries, thus decreasing the computational load considerably compared to the FEM. For a location on smooth boundary surfaces, ϕ is formulated as [56]

$$\phi(\vec{r}) = \frac{2\sigma_s}{\sigma_i^- + \sigma_i^+} \phi_0(\vec{r}) - \frac{1}{2\pi} \sum_{k=1}^K \frac{\sigma_k^- - \sigma_k^+}{\sigma_i^- + \sigma_i^+} \int_{S_k} \phi(\vec{r}') \frac{(\vec{r} - \vec{r}')}{\|\vec{r} - \vec{r}'\|^3} d\vec{S}_k, \quad \vec{r} \in S_i \quad (3.4)$$

where ϕ_0 is the potential due to the primary current distribution \vec{J}_p if the conducting medium for the source were infinite in extent and has the conductivity σ_s . For primary current sources inside the volume conductor, ϕ_0 is

$$\phi_0(\vec{r}) = \frac{1}{4\pi\sigma_s} \int_{V'} \frac{\vec{J}_p(\vec{r}') \cdot (\vec{r} - \vec{r}')}{\|\vec{r} - \vec{r}'\|^3} dV'. \quad (3.5)$$

Thus, to calculate the magnetic field $\vec{B}(\vec{r})$ due to source currents in a volume conductor, one has to solve Eqs. 3.5, 3.4, 3.3 and finally Eq. 3.2.

When modeling the head using BEM, one typically uses either only a single boundary corresponding to the surface of the intracranial volume or three boundaries dividing the head into brain, skull and scalp. Using such a *multi-compartment model* provides more accurate results without any significant disadvantages compared to single-compartment model [57]. The geometries of these boundaries are determined through the segmentation of MR images of the subject's head. If MR images are not available, one may instead use template volume conductor models based on population-wide studies or a simple spherical model.

Pragmatically speaking, most heads can be approximated reasonably well by a sphere. The use of a spherical model also demonstrates why MEG has poor sensitivity to sources at the gyral crowns [58]; radially-oriented current sources in a spherical volume conductor generate no magnetic field outside the sphere. In reality, this is not strictly true due to the deviation of a real head from a sphere, but rather holds as a rule of thumb: while the sensitivity is not strictly zero, MEG has poor sensitivity to quasi-radially oriented sources.

The conductivity values used for the different compartments come from the findings of several studies ranging from in-vitro to carcass examinations of tissue conductivity [59, 60, 61, 62, 63]. The conductivity of the skull is especially hard to pinpoint as the skull consists of several layers, which can be difficult to segment accurately from MR images. Fortunately, the conductivity of the skull does not affect MEG to the same degree as in EEG [64].

In addition to the skull, the layer of corticospinal fluid between the skull plays a significant role in modeling of cortical sources as it functions as a high-conductivity layer which allows for the volume current loops to close without going through the comparatively high-resistance skull. This effect is especially important in EEG, although it is not wholly insignificant in MEG [65]. Thus, including the CSF as an additional, fourth BEM compartment may be advantageous if the CSF compartment can be properly identified in the MR images. Alternatively, one can approximate the effect of the CSF by adjusting the conductivity value of the skull compartment [65].

3.3.2 The inverse problem

Most traditional methods to estimate the source distribution $\hat{\mathbf{x}}$, in their most general form (the generalized linear inverse), [66] can be stated as

$$\hat{\mathbf{x}} = \mathbf{K}_{\mathbf{x}} \mathbf{G}^{\top} \mathbf{K}_{\mathbf{y}}^{-1} \mathbf{y} = \mathbf{K}_{\mathbf{x}} \mathbf{G}^{\top} (\mathbf{G} \mathbf{K}_{\mathbf{x}} \mathbf{G}^{\top} + \mathbf{K}_{\mathbf{n}})^{-1} \mathbf{y}, \quad (3.6)$$

where $\mathbf{K}_{\mathbf{x}}$ is the source covariance matrix, $\mathbf{K}_{\mathbf{n}}$ is the noise covariance matrix and $\mathbf{K}_{\mathbf{y}} = \mathbf{G} \mathbf{K}_{\mathbf{x}} \mathbf{G}^{\top} + \mathbf{K}_{\mathbf{n}}$ is the measurement covariance matrix. The different inversion methods used in MEG and EEG differ mainly in the way that the source covariance matrix is specified or estimated.

The minimum-norm estimate

The minimum-norm estimate is very similar to Eq. 3.6. In its “classical” form, it can be expressed simply by setting $\mathbf{K}_\mathbf{x} = \mathbf{I}$ and introducing the regularization parameter λ^2 [67, 68]:

$$\hat{\mathbf{x}} = \mathbf{G}^\top (\mathbf{G}\mathbf{G}^\top - \lambda^2 \mathbf{K}_\mathbf{n})^{-1} \mathbf{y}. \quad (3.7)$$

Although this prior assumption has no immediate physiological basis, MNE has gained significant popularity due to its computational simplicity. The regularization parameter λ^2 is set according to the (assumed) ratio between source and noise covariances, i.e. the SNR. Often, the formula

$$\lambda^2 = \frac{\text{tr}(\tilde{\mathbf{G}}\tilde{\mathbf{G}}^\top)}{N\overline{\text{SNR}}^2} \quad (3.8)$$

presented by Lin et al. [69] is used, where $\text{tr}(\cdot)$ denotes the trace operator, $\tilde{\mathbf{G}} \equiv \mathbf{K}_\mathbf{y}^{-1/2} \mathbf{G}$ is the whitened gain matrix, N is the number of sensors in the measurement and $\overline{\text{SNR}}$ is the assumed mean (amplitude) SNR.

In practice, MNE leads to large, diffuse estimates that tend to overestimate the spatial spread of sources (see Fig. 3.5). Despite these drawbacks MNE is a robust and widely employed inversion method.

Eq. 3.7 is known to be biased towards superficial areas since they tend to explain signal very well due to the close proximity to the sensors. To compensate for this bias, one can apply depth-weighting [69] by modifying $\mathbf{K}_\mathbf{x}$. Note that other biases, i.e. priors, can be introduced to the estimate in this manner. Alternatively, one can apply noise-normalization methods [70, 71], in which the MNE result is divided by that produced by noise only.

Beamforming

Beamformers are adaptive spatial filters constructed using estimates of the data covariance $\mathbf{K}_\mathbf{y}$ that, for each source location, tries to pass source activity at that location, while attenuating contributions from all other locations. By designing filters for each location in the brain, one can achieve a spatial map of neural activity by depicting filter output as a function of passband location [72, 73, 74].

Beamformers can also be expressed in the form of Eq. 3.6, with the assumption that the sources are independent, i.e. that $\mathbf{K}_\mathbf{x} = \text{diag}(\sigma_i^2)$, where σ_i^2 is the source variance of the i th source [66]. Inserting this assumption into Eq. 3.6, the estimate for each source becomes

$$\hat{\mathbf{x}}_i = \sigma_i^2 \mathbf{G}_{:,i}^\top \mathbf{K}_\mathbf{y}^{-1} \mathbf{y}, \quad (3.9)$$

where $\mathbf{G}_{:,i}$ is the sensitivity of all sensors to the i th source. If we next estimate the source variance in terms of the data covariance matrix as $\sigma_i^2 = \mathbf{G}_{:,i}^\top \mathbf{K}_\mathbf{y} \mathbf{G}_{:,i}$, we arrive at the expression for the *linearly constrained minimum-variance* (LCMV) beamformer

$$\hat{\mathbf{x}}_i = (\mathbf{G}_{:,i}^\top \mathbf{K}_\mathbf{y}^{-1} \mathbf{G}_{:,i})^{-1} \mathbf{G}_{:,i}^\top \mathbf{K}_\mathbf{y}^{-1} \mathbf{y}. \quad (3.10)$$

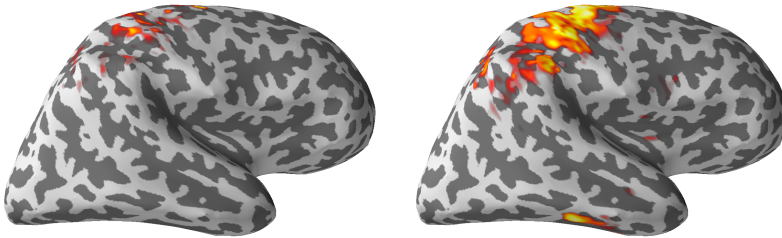


Figure 3.5. LCMV beamformer (left) and MNE (right) source estimates on a cortical source space for the same MEG data. The cortical surface has been ‘inflated’ to allow for easier visualization.

Although one could directly use Eq. 3.10 to estimate the activity of all sources across the source space, at deeper locations measurement noise will drown out any genuine sources due to low SNR. As such, the estimate will be biased towards deeper sources and needs to be normalized. Starting at the prior assumption of Eq. 3.9, the expected estimated source power is

$$E(\hat{\mathbf{x}}_i^2) = \sigma_i^4 \mathbf{G}_{:,i}^\top \mathbf{K}_y^{-1} \mathbf{G}_{:,i}. \quad (3.11)$$

When the measurement is composed purely of noise, i.e. $\mathbf{y} = \mathbf{n}$, the expected source power is

$$E(\hat{\mathbf{x}}_i^2 | \mathbf{y} = \mathbf{n}) = \sigma_i^4 \mathbf{G}_{:,i}^\top \mathbf{K}_y^{-1} \mathbf{K}_n \mathbf{K}_y^{-1} \mathbf{G}_{:,i}. \quad (3.12)$$

Forming a ratio of these two quantities, we arrive at the pseudo-Z-score

$$Z_i^2 = \frac{E(\hat{\mathbf{x}}_i^2)}{E(\hat{\mathbf{x}}_i^2 | \mathbf{y} = \mathbf{n})} = (\mathbf{G}_{:,i}^\top \mathbf{K}_y^{-1} \mathbf{K}_n \mathbf{K}_y^{-1} \mathbf{G}_{:,i})^{-1} \mathbf{G}_{:,i}^\top \mathbf{K}_y^{-1} \mathbf{G}_{:,i} \quad (3.13)$$

that is termed the *neural activity index* [75, 76]. Many other normalization methods exist, for a review, see [73].

A frequency-domain variant of beamforming called *dynamic imaging of coherent sources* (DICS) also exists [77], in which the covariance matrices in Eq. 3.13 are replaced with cross-spectral density matrices to locate frequency-specific sources.

As beamformers assume that all sources are independent, typical beamformers cannot separate sources with correlated time-courses. Instead, they will result in erroneous power and location estimates. Beamformers typically result in relatively focal source estimates (see Fig. 3.5), and they can be used either with cortical source spaces or volumetric source spaces corresponding to the entire brain. The choice of source space has somewhat different implications when using beamformers compared to, e.g. MNE, as the filters specifically attempt to suppress any activity from outside the source space.

Dipole fitting

Arguably the simplest prior that can be used to make the inverse problem well-posed is to assume that the measured magnetic field is caused by a single *equivalent current dipole* (ECD) representing a small, focal activation of cortical tissue. For dipole fitting, a source space is not always used; instead the dipole position and orientation may be unconstrained within the volume conductor. In that case, least-squares minimization of the error between the measured magnetic field and the magnetic field caused by the estimated dipolar activation is typically used to find the ECD. As the measured magnetic field varies non-linearly with the position of the source, a non-linear search is used to adjust the position and moment of the ECD. This single-dipole model can also be expanded to include several dipoles, although the correct estimation of several dipoles can be difficult, especially if they are temporally correlated [78].

3.3.3 Co-registration

In order to compute \mathbf{G} and thus to enable source modeling, one needs to know the position and orientation of the sensors in relation to the brain. Since we don't have any direct external knowledge of the geometry of the brain, we rely on structural images of the brain. Most commonly, the structural image in question is a T1-weighted MR image, which will need to be co-registered to the MEG data, i.e. the data from both modalities need to be transformed to a common coordinate system. Accurate co-registration of MEG and MRI is critical for reliable source modeling as shown in several studies concerning conventional SQUID-based MEG [79, 80, 81, 82] and EEG [83, 84]. In Publication I, it was also shown that for on-scalp MEG to have benefits over conventional MEG, accurate co-registration is needed.

Co-registration is usually based on a set of *fiducial points* that can be identified in both data sets and thereafter aligned [85, 86]. The fiducials most commonly used on the head are the nasion and the preauricular points as defined in the 10-20 EEG electrode system [87].

The current standard co-registration method in SQUID-based MEG relies on the combination of small wire-wound coils called *head position indicator* (HPI) coils [88] attached to the participant's head and a pen-like electromagnetic 3D digitizer. Prior to MEG measurements, the positions of the HPI coils as well as a set of fiducial points on the head are digitized. To localize the HPI coils with respect to the MEG sensors, known currents are driven into the coils either sequentially or at different frequencies prior to or continuously during MEG measurements [89]. A magnetic dipole model representing each coil is fitted to the acquired MEG sensor signals to localize the coils in the MEG device coordinate system. Finally, the actual co-registration is performed by aligning the HPI-coil locations as determined by the MEG system with those determined by digitization and aligning the digitized anatomical landmarks with the same landmarks in the MR image.

The accuracy of the standard co-registration method can be improved by digitizing not only a small number of fiducial points but also a larger set of points on the head surface [90]. Due to the need to manually digitize each point, their number is usually limited to some hundreds. For the same reason, the number of HPI coils is typically no more than five. Several variants of this method have also been developed. These include e.g. bite-bars [80] with HPI coils for a more easily reproducible co-registration when compared to HPI coils positioned on the scalp. The disadvantage of this technique is that all HPI coils are then positioned at the front of the head, which can magnify the effect of small errors. Localizing the HPI coils reliably requires a large number of sensors covering large parts of the scalp and requires the sensor array geometry to be well-known. Thus, using the standard HPI-based co-registration method with early-stage on-scalp MEG systems with only a few channels is not feasible.

With optical scanning methods, one can obtain orders of magnitude more points in significantly less time than when manually digitizing HPI coils. During the past decade, faster or more accurate digitization and co-registration methods have been demonstrated for MEG and EEG [79, 83, 91, 92, 93, 94]. With the ongoing development and commoditization of consumer-grade 3D scanners, the use of optical co-registration has become increasingly attractive. In Publication II, we developed an optical co-registration method applicable for on-scalp MEG.

An entirely different co-registration methodology was used by Troebinger et al. [95], who created individualized 3D-printed head casts based on optical scans of the head shape and MR images, which fit into the helmet of the MEG system. Using these head casts together with MR-visible fiducial markers, accurate co-registration is possible and head motion during measurements is minimized. Additionally, the co-registration error between measurement sessions was also greatly diminished. The same approach has later been applied to OPM-based MEG systems in order to circumvent the inability to use HPI coils [96]. The most obvious disadvantage of using individualized head casts is that they must be custom-made to fit each individual. Thus, head casts are ill-suited for larger-scale studies or clinical use. A clever way to invert the conventional HPI coil co-registration process was developed by Pfeiffer et al. [97, 98]. In this variant of the conventional method, a large number of HPI coils with accurately known locations and orientations are used to localize the sensors.

In current SQUID-based MEG systems, the sensors are rigidly mounted, meaning that their positions in relation to each other and their orientations are known. In an on-scalp MEG system in which the positions of sensors are freely adjustable to the head size and shape of the subject, co-registration becomes more challenging due to the additional degrees of freedom involved; instead of localizing a single known set of sensors one needs to independently localize each sensor. Individually localizing the sensors will also change the type of co-registration error present; co-registration error in current SQUID-based MEG systems with rigid sensor arrays is systematic in nature. In on-scalp MEG systems with adaptable sensor arrays sensor-wise co-registration errors can also

occur. In Publication I, we examined how such sensor-wise co-registration error affects source estimation performance.

3.4 Optically-pumped magnetometers (OPMs)

Recent advances in atomic physics and diode lasers has enabled the development of compact *atomic magnetometers*, known as *optically-pumped magnetometers* (OPMs) within the biomedical community, with high enough sensitivity to measure biomagnetic signals such as MEG [99, 100]. The prime advantage of OPMs over current SQUID sensors used in MEG is that they do not require any cryogenic cooling. OPMs can be miniaturized and potentially mass-produced at low cost [101]. The absence of cryogenic cooling enables the placement of sensors much closer to the neuromagnetic sources in the brain, thus boosting the SNR and spatial resolution considerably [102, 103]. Furthermore, it significantly opens MEG system design options in terms of sensor array geometry, allowing for wearable sensor arrays [96] as well as small, application-specific systems.

The general principle in optical magnetometry, in very broad terms, is that light is used to measure the response of *atomic angular momentum* to the presence of a magnetic field [104]. Atomic magnetic moments emerge due to the magnetic moments associated with the intrinsic *spin* of electrons, atomic nuclei and orbital motion of electrons. When an external magnetic field \vec{B} is applied a torque acts on the atoms, causing the angular momentum to *precess* around \vec{B} at the Larmor frequency $\omega_L = \gamma|\vec{B}|$, where γ is the *gyromagnetic ratio* of the atom species in question. Applied light interacts with the atomic medium, exchanging angular momentum. Thus, the angular momentum of the light is affected by the angular momentum of the atomic medium, which in turn is driven by the precession caused by the external magnetic field. Using this relation, the precession of atomic angular momentum can be observed optically through the changes in intensity and polarization of light propagating through the atomic medium. In the following sections, this physical principle of operation will be covered in more detail following the same structure as used by Tierney et al. [105] and Iivanainen [106].

3.4.1 Physical principle of operation

Atom energy levels & angular momenta

Spin (\vec{S}) is a particular form of (quantum) angular momentum which is intrinsic to some elementary particles, such as the electron. Another form of angular momentum present in the atom include the orbital angular momentum \vec{L} which can be classically interpreted as the orbital motion of electrons. Together, \vec{S} and \vec{L} form the total electron angular momentum $\vec{J} = \vec{L} + \vec{S}$. The total atomic angular momentum $\vec{F} = \vec{J} + \vec{I}$ consists of the sum of the electron angular momentum and

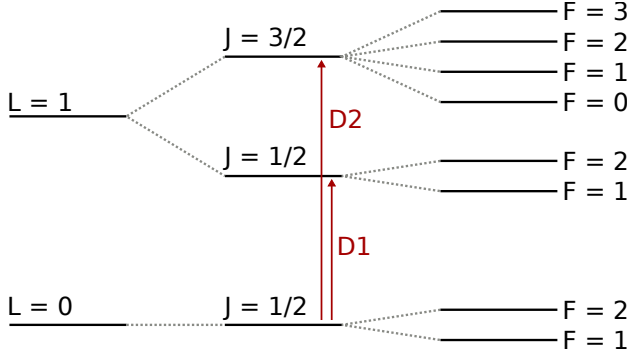


Figure 3.6. Energy level diagram of Rubidium-87, showing the lowest energy levels (not to scale). The fine and hyperfine structure splittings are also shown as well as the two lowest level transitions D1 and D2. The Zeeman sublevel splitting is not shown.

the nuclear angular momentum \vec{I} . The *quantum numbers* (represented by the scalars S , L , J , I and F) for these angular momenta can only assume certain values that define the possible values of the total atom angular momentum and also energy level structure. The relation between the quantum number and the momentum is given by $|\vec{S}| = \sqrt{S(S+1)}\hbar$, which holds for all the involved momenta.

Alkali metal atoms are useful for a variety of applications ranging from atomic clocks to magnetometers since they have a single valence electron that is easily manipulated. The atom energy structure can be well approximated by considering only the valence electron and the nucleus, thus ignoring the electrons in the inner energy shells. Here we will consider Rubidium-87 (^{87}Rb) as an example, and its energy level structure is shown in Fig. 3.6. The spin angular momentum of the single valence electron is given by $S = 1/2$, and L can take integer values from 0 to 4 [105].

Interactions between the electron spin and its orbital motion results in *fine structure splitting* of the atom energy levels. The fine structure results in permitted values for J being integers between $|L - S|$ and $L + S$. These can be thought of as states with the spin and orbital angular momenta lying anti-parallel and parallel, respectively [107]. The fine structure is further split by the *hyperfine structure splitting* due to interaction between the total electron angular momentum \vec{J} and the nuclear angular momentum \vec{I} . Similarly to the fine structure split, the total atom angular momentum quantum number F can take integer values between $|I - J|$ and $I + J$. For ^{87}Rb , the nuclear angular momentum quantum number is $I = 3/2$.

Finally, when exposed to a magnetic field, the hyperfine structure is further split into *Zeeman sublevels* with projections m_F being integer values between $-F$ and F . The energy splitting ΔE_L between the Zeeman sublevels is linearly dependent on the field strength and causes the spin precession about the magnetic field at the Larmor frequency $\omega_L = \Delta E_L/\hbar = \gamma|\vec{B}|$ [107].

Optical pumping

Light is quantized into *photons*, which carry an intrinsic angular momentum (spin) equal to $\pm\hbar$ ($s=1$) and the energy $E = \hbar\omega = \hbar c/\lambda$, where λ is the wavelength of the photon and c is the speed of light in a vacuum. The helicity, or projection of the intrinsic angular momentum (spin) on the direction of momentum is either right-handed (\hbar) or left-handed ($-\hbar$). These photons are referred to as being *circularly polarized*. A photon that is *linearly polarized* is in a superposition of equal amounts of the left-handed and right-handed states.

Atoms can absorb photons to transition electrons from their ground state to an excited state and correspondingly emit photons when excited electrons spontaneously transition to lower energy states. When an atom emits or absorbs a photon, energy and angular momentum must be conserved; thus, the energy of the photon (either absorbed or emitted) must correspond to the energy-difference of the states involved in the transition. In ^{87}Rb , there are two transitions from the ground state $L = 0$ to the first excited state $L = 1$ due to the fine structure. These are referred to as D1 (transition energy corresponds to 795 nm light) and D2 (transition energy corresponds to 780 nm light), respectively. These two transitions are commonly used to manipulate the atoms in devices such as optically-pumped magnetometers by using lasers specifically tailored for these transition wavelengths. The conservation of angular momentum dictates that only some transitions are possible; for example, an atom in the state $L = 0$, $F = 2$, $m_F = 2$ cannot absorb a right-handed (σ^+) photon with a wavelength corresponding to the D1 transition as the angular momentum of the photon cannot be conserved (there is no $m_F = 3$ state).

Optical pumping [108] refers to the application of circularly polarized, resonant light to move all atoms in an ensemble into the same spin state, thus creating net *spin polarization*. Optical pumping of ^{87}Rb is illustrated in Fig. 3.7. When using σ^+ -polarized light, a photon adds $+1$ to m_F as the valence electron is excited to the $L = 1$ state. As the electron spontaneously decays back to the ground state, it emits a photon with random polarization. The m_F value in the ground state is then set to conserve angular momentum: the ground state m_F value is thus either the same as in the excited state (linear polarization) or ± 1 (right- or left-handedly circularly polarization). As optical pumping continues, the combination of continuous added angular momentum in excitation and random angular momentum change in decay will lead all atoms in the ensemble to be trapped in the $F = 2$, $m_F = 2$ “end state”. As long as no relaxation occurs, the atoms can no longer absorb further photons. Light now passes through the atoms without absorption and the atoms coherently precess about the external magnetic field.

Relaxation and the spin-exchange relaxation-free regime

Unfortunately, the spin polarization is not perpetually preserved. As the atoms collide with each other or the walls of the cell they are confined in, the spin polarization relaxes as atoms are moved away from the end state. The atom–

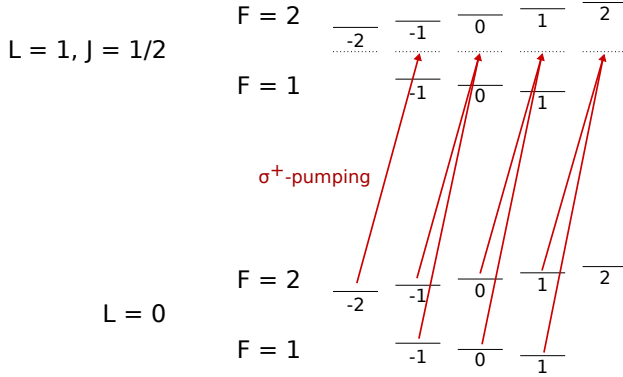


Figure 3.7. Zeeman-sublevel energy level diagram of Rubidium-87, showing how optical pumping with σ^+ light tuned to the D1 transition moves an atom to the $m_F = 2$ state. Inspired by Fig. 2.8 of [107].

atom collisions can be divided into *spin-destruction* (SD) and *spin-exchange* (SE) collisions. In SD collisions, angular momentum is transferred to the orbital angular momentum, and the total spin is not conserved. In SE collisions, total spin is conserved but the electron spin direction of the colliding atoms can be flipped. In other words, the colliding atoms can move between hyperfine levels, which means that the Zeeman sublevels are also redistributed. Atoms in ground-state $F = 1$ and $F = 2$ hyperfine levels precess with approximately the same frequency, but in opposite directions [107].

In high ambient magnetic fields, SE collisions are typically the primary reason for spin relaxation. As the magnetic field approaches zero, the Larmor frequency and the energy difference between Zeeman sublevels also disappear, and spin-exchange no longer affects the polarization lifetime. The effect of SE collisions also changes when the atom density becomes so high that spin-exchange collisions happen at a much faster rate than the Larmor frequency. In this *spin-exchange relaxation free* (SERF) regime, the atoms spend a very short time in each hyperfine state, leading to a coherent precession due to the fact that a larger proportion of the atoms are in the upper $F = 2$ hyperfine state, which has a larger number of Zeeman sublevels [107]. In the SERF regime, a strong spin polarization can be maintained as the relaxation rate is now governed by the much smaller SD collisions and other relaxation factors. The SERF regime idea was first presented in the 1970s [109, 110], and only demonstrated in a magnetometer with much improved sensitivity several decades later [111].

Atom ensemble behavior

The spin polarization \vec{P} of an atom ensemble in the SERF regime precesses about an external magnetic field. The macroscopic behavior of this polarization, and how it relates to the magnetic field, can be described using the Bloch equations [112]. \vec{P} is coupled to the magnetic field according to the single Bloch equation

[113, 114, 115]

$$\frac{\partial \vec{P}}{\partial t} = \gamma \vec{P} \times \vec{B} - \frac{1}{T} \vec{P} + \frac{1}{T_p} (\vec{P}_0 - \vec{P}), \quad (3.14)$$

where the first term corresponds to the magnetic field coupling, the second term is the total spin relaxation governed by the relaxation time T and the third term describes the optical pumping, which attempts to maintain the equilibrium polarization \vec{P}_0 with the pumping rate $\frac{1}{T_p}$. Using the substitutions $\frac{1}{\tau} = \frac{1}{T} + \frac{1}{T_p}$ and $\vec{P}'_0 = \vec{P}_0 \frac{T}{T_p + T}$, we can simplify Eq. 3.14 as

$$\frac{\partial \vec{P}}{\partial t} = \gamma \vec{P} \times \vec{B} + \frac{1}{\tau} (\vec{P}'_0 - \vec{P}), \quad (3.15)$$

which now incorporates the effects of pumping and relaxation into a single term. The steady-state solution for Eq. 3.15, assuming that the optical pumping is along the x -axis (i.e. $\vec{P}'_0 = P'_0 \hat{e}_x$) is

$$P_x = \frac{P'_0(1 + \gamma\tau B_x^2)}{1 + (\gamma\tau)^2(B_x^2 + B_y^2 + B_z^2)} \approx \frac{P'_0}{1 + (\gamma\tau B_z)^2} \quad (3.16)$$

$$P_y = \frac{(-\gamma\tau B_z + (\gamma\tau)^2 B_x B_y) P'_0}{1 + (\gamma\tau)^2(B_x^2 + B_y^2 + B_z^2)} \approx \frac{-\gamma\tau B_z P'_0}{1 + (\gamma\tau B_z)^2} \quad (3.17)$$

$$P_z = \frac{(\gamma\tau B_z + (\gamma\tau)^2 B_x B_z) P'_0}{1 + (\gamma\tau)^2(B_x^2 + B_y^2 + B_z^2)} \approx 0, \quad (3.18)$$

where the right-side approximation corresponds to no off-axis magnetic field being present ($B_x = B_y = 0$).

The polarization curves (as a function of the z -axis component of the magnetic field B_z , shown in Fig. 3.8) defined by these equations have an absorptive (P_x) and dispersive (P_y) shape. When the off-axis magnetic field is not strictly zero, there will be further effects that complicate the response to magnetic field by mixing the different components and introducing non-linearities [107, 116].

The dispersive lineshape of Eq. 3.17 is linear when the magnetic field is near zero. Thus, one needs to monitor P_y to readout a signal proportional to B_z . To this end, a linearly polarized *probe laser* with the beam perpendicular to the pump laser can be used. Since the probe laser photons have arbitrary helicity (linear polarization), they disrupt the spin polarization when they are absorbed. In order to avoid this effect, the probe laser should be slightly detuned from the transition used in order to reduce the probe absorption [107].

By applying a small sinusoidal modulation field $B_1 \cos(\omega t)$ with a frequency $\omega \gg 1/\tau$ to the atomic medium, one can define a primary sensitive axis for the magnetometer, as well as reduce technical and $1/f$ noise. The modulation field will also modify the polarization response, moving the dispersive lineshape from P_y to P_x . Thus, the pump laser also acts as a probe, and a separate probe laser is not necessary for signal readout. The steady-state solution is no longer valid

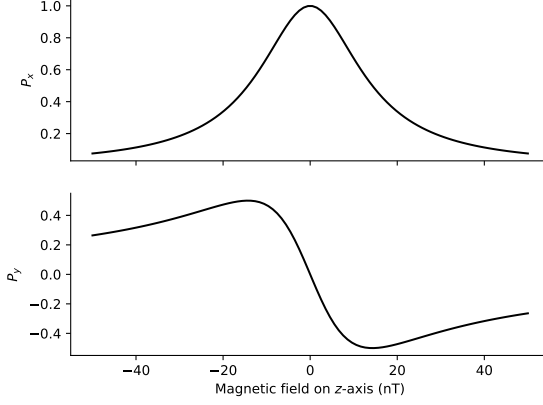


Figure 3.8. Spin polarization along x - and y -axes as a function of magnetic field along the z -axis. Graphs are computed with semi-realistic values for ^{87}Rb ; $\gamma = 7 \text{ Hz/nT}$, $\tau = 0.01 \text{ s}$ and $P'_0 = 1$.

due to the fast modulation, but the solution can be presented in the form of a Fourier series, which for harmonics with even order m is [113, 114]

$$P_x = P'_0 J_0 \left(\frac{\gamma B_1}{\omega} \right) J_m \left(\frac{\gamma B_1}{\omega} \right) \frac{1}{1 + (\gamma \tau B_z)^2} \cos(m\omega t) \quad (3.19)$$

and for odd m is

$$P_x = P'_0 J_0 \left(\frac{\gamma B_1}{\omega} \right) J_m \left(\frac{\gamma B_1}{\omega} \right) \frac{\gamma \tau B_z}{1 + (\gamma \tau B_z)^2} \sin(m\omega t), \quad (3.20)$$

where J_m are m th-order Bessel functions of the first kind. Even and odd harmonics result in absorptive and dispersive lineshapes, respectively. For P_y , the solutions are the same as for P_x , except with the odd and even harmonics swapped.

Just as with 3.17, the dispersive lineshape of 3.20 is linear when the magnetic field is near zero. Thus, after demodulation of the periodic term, the readout signal V (which is typically a voltage signal from a polarimeter or photodiode) will be of the form

$$V = A \gamma \tau B_z, \quad (3.21)$$

where $A \gamma \tau$ is the linear gain [105]. Here, A is a new term introduced that incorporates the Bessel function terms as well as P'_0 . As seen from Eq. 3.21, the gain and thus also SNR of the magnetometer signal is dependent on γ and τ , which are dependent on spin polarization and atom density. The gyromagnetic ratio γ grows as the spin polarization P'_0 approaches unity [111, 117]. The relaxation time τ also grows when spin polarization increases. However, there is an inherent trade-off between sensor bandwidth and sensitivity; the polarization is insensitive to magnetic field changes with $\omega \gg 1/\tau$, and the frequency response

of the spins can be approximated as a first-order low-pass filter with the -3 dB-cutoff at $1/\tau$ [100].

3.4.2 Sensor components

The core of an OPM consists of a vapor cell typically filled with alkali-metal atoms, e.g. Rubidium [100], Potassium [115] or Cesium [118]. Helium may also be used [119, 120], although its energy level-structure differs from that of alkali atoms. The vapor cell dimensions can vary according to the application; for small form-factor sensors, mm-scale cells have been used [121], while other sensors with extremely low noise levels use vapor cells with sidelengths of several centimeters for each dimension [122]. One can also employ a single large vapor cell in conjunction with multiple laser beams (possibly split from the same source), thus creating a sensor array with a common vapor cell [123, 124]. The vapor cell usually contains a buffer gas, e.g. nitrogen, which reduces the diffusion of the alkali atoms. Additionally, the cell walls may be coated with anti-relaxation coatings [125, 126], which, as the name implies, reduce the spin relaxation caused by atom-wall collisions.

To achieve the high atom density required to reach the SERF regime, the vapor cell is heated to 100–200°C, depending on the atom species (Rubidium requires higher temperatures than Cesium to achieve good magnetometer performance). The cell is heated either using resistive heaters (see e.g. [100]) or optically using a heating laser whose wavelength is blocked by a filter at the vapor cell walls, thus heating the filter and the cell [121].

As the magnetic field must be low (on the order of tens of nanoteslas) in order to achieve SERF operation, most OPM sensors include in-sensor coils which are used to cancel the field within the vapor cell, either using a one-time procedure when starting the sensor, or using negative feedback. Some sensor designs also utilize modulation fields in order to simplify the signal readout, and typically the same coils are used for this purpose as well. Fig. 3.9 shows a simplified schematic of such a sensor.

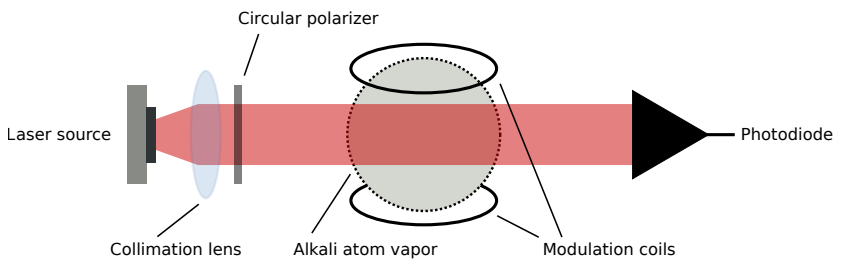


Figure 3.9. Simplified schematic of a SERF OPM utilizing field modulation.

The pump lasers used for SERF OPMs are usually vertical-cavity surface-emitting lasers (VCSELs), as they provide a narrow linewidth and suitable optical power (100 μW – 1 mW) at affordable unit prices. Another alternative is

to use a single high-power laser for several sensors using optical fibers and a fiber splitter [127, 128]. Regardless, the pump laser beam is typically collimated into a parallel beam, after which a quarter-wave plate is used to produce circular polarization. In sensors utilizing a separate probe laser for signal readout, the probe is typically perpendicular to the pump laser although this is not strictly required [129].

Many times, the optical path is not straight as in Fig. 3.9; in miniature sensors, small mirrors are often used to make the sensor fit a small footprint. Another consideration is that the pump laser current may produce magnetic noise, and thus it shouldn't be too close to the vapor cell.

3.4.3 OPM-based MEG

To date, most OPM-based MEG measurements have been proof-of-concept measurements of well-known MEG responses (e.g. [100, 120, 121, 123, 130, 131, 132, 133, 134]). In some cases, these measurements have been performed using a single or a small number of very large sensors, which due to their size have very good noise performance. However, these sensors are not suitable for use in multi-channel sensor arrays. At the other extreme, invasive OPM-MEG measurements using miniature sensors have been performed on rats [135].

In the recent years, there has been a surge of publications using small or moderate-sized sensors in multi-channel systems (e.g. [96, 116, 128, 136, 137], Publication III). Some of these systems have utilized commercially available SERF OPMs [138]. Due to the commercial availability of sensors, OPM-MEG has matured from being developed exclusively in physics labs to also being used by more physics- and technical-minded neuroscientists. As a consequence, there has also been significant development in the OPM-MEG systems that surround the sensors, bringing OPM-MEG closer to being easily used for neuroscientific applications (and a long way down the road, clinical use). These systems developments include new sensor support mechanisms (e.g. [96, 116, 139], Publication II), small person-sized shields [44, 128], active shielding and interference suppression methods [116, 140] as well as new co-registration methods ([139, 141], Publication II) that enable source estimation. Further novel developments include the advent of wearable MEG [96] and virtual reality-enabled OPM-MEG [142], both of which can open new paradigms for neuroscientific research. Recently, the first whole-head OPM-MEG system, comprising 49 sensors, was demonstrated [143].

3.5 Magnetic field modeling using stream functions

In MEG and OPM sensor design, coils are needed for magnetic field control and modulation fields. Using surface currents, one can model coil current patterns that generate desired magnetic fields. Other applications of surface

currents include modeling eddy currents in conducting sheets, which requires the calculation of the coupling between the external field and the currents as well as the inductive effects of the currents within the conductor [144, 145]. Such modeling is also useful in computing the magnetic noise arising from thermal fluctuations [146, 147, 148]. Finally, through such field calculations, surface currents can be used as equivalent sources in reconstruction and interpolation of magnetic fields, e.g., in geo- [149, 150] and biomagnetism [151].

A current density is often represented using a set of basis functions. For currents on simple domains (such as planes, cylinders, toroids, or spheres), basis functions can be formed analytically [146, 152, 153, 154, 155, 156, 157]. Pissanetzky [158] introduced a general *stream-function* representation of the surface-current density on arbitrary surfaces, which discretizes the current on triangle surface meshes in a manner similar to FEM and BEM.

Within the field of magnetic resonance imaging (MRI), triangle mesh-based stream-function methods have been applied to magnetic field modeling and coil design since the early 1990s [144, 158, 159, 160, 161]. Similar methods have also been used in plasma physics [162]. More recently, the same principles have been used in the design of coils for transcranial magnetic stimulation (TMS) [163, 164] as well as magnetic nanoparticle imaging [165]. Finally, these methods have been used in OPM-based MEG to design large field nulling coils within the MSR, which then allows for wearable OPM-MEG [96, 140].

In Publication IV, we presented an open-source Python software package for magnetic field modeling and coil design, `bfieldtools`. Publication IV focuses on describing the software package itself and demonstrates its usage through several examples. A more thorough treatment of the underlying physics and computational aspects is given in an accompanying publication by Mäkinen et al. [166]. This section will cover the basics of stream-function-based magnetic field modeling and some of the associated computations, followed by some more application-specific topics. These topics include coil design for OPM-MEG as well as using equivalent surface current modeling to interpolate magnetic fields.

3.5.1 Computations using the discrete stream function

A scalar stream function $\psi(\vec{r})$ can be used to represent any divergence-free current density $\vec{j}(\vec{r})$ on an arbitrary surface as [144, 158]

$$\vec{j}(\vec{r}) = \nabla_{\parallel} \psi(\vec{r}) \times \hat{n}(\vec{r}), \quad (3.22)$$

where \vec{r} is the position on the surface, \hat{n} is the unit surface normal, and ∇_{\parallel} is the tangential gradient operator [167]. For convenience, the operator $\nabla_{\parallel}(\cdot) \times \hat{n}$ can be termed the *rotated gradient*.

For practical use, the stream function can be discretized as a piece-wise linear function onto a triangle mesh. Compared to analytic methods that require specific symmetries for the source-current distributions, the use of triangle meshes as source domains makes the method more widely applicable by providing the

user with considerable geometrical freedom.

Triangle discretization

The triangle mesh discretization is based on approximating the stream function linearly on the face of each triangle as in FEM-based models, and as illustrated in Fig. 3.10. A piece-wise linear stream function is defined on the surface using so-called hat functions, which are defined as having the value one at a single vertex and falling linearly to zero at the edges of the triangles neighboring the vertex. The stream function ψ can then be represented as a linear combination of the hat functions h_i with weights s_i

$$\psi(\vec{r}) = \sum_i s_i h_i(\vec{r}). \quad (3.23)$$

The stream function weights s_i can be collected in a column vector $\mathbf{s} \in \mathbb{R}^{N_v \times 1}$. Linear operations on the stream function can thus be represented as matrices operating on \mathbf{s} . For convenience, \mathbf{s} will simply be referred to as the stream function from here on.

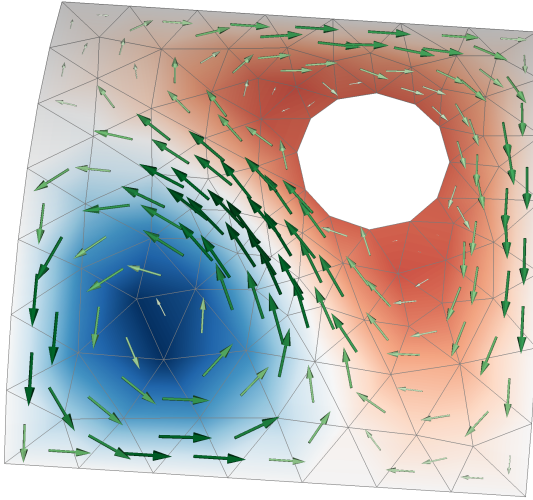


Figure 3.10. An example stream function (red-blue colormap) and its rotated gradient, i.e. the surface current density (arrows; white-green colormap), on a surface mesh with a hole in it. The surface normal is oriented up towards the reader. The white-green colormap and the size of the arrows indicate the magnitude of the current density. The stream function colormap is linear and zero-centered. Red corresponds to negative and blue to positive values.

The surface-current density is obtained as the rotated gradient of the piece-wise linear stream function, which makes it constant on each triangle face [166]. Thus, we can express the current density $\mathbf{j} \in \mathbb{R}^{N_f \times 3}$ on the faces of the mesh in shorthand notation (see Publication IV) using the rotated gradient matrix $\nabla^\perp \in \mathbb{R}^{N_f \times 3 \times N_v}$ as

$$\mathbf{j} = \nabla^\perp \mathbf{s}. \quad (3.24)$$

Coupling matrices

The magnetic field and other related quantities (such as the magnetic potentials) at given points are linear functions of the stream function. For example, knowing the coupling $\mathbf{C}_{\bar{B}} \in \mathbb{R}^{N_p \times 3 \times N_v}$ between the stream function values $\mathbf{s} \in \mathbb{R}^{N_v \times 1}$ defined at the N_v vertices of the mesh and the magnetic field $\mathbf{B} \in \mathbb{R}^{N_p \times 3}$ at the N_p field evaluation points $\mathbf{r} \in \mathbb{R}^{N_p \times 3}$, the magnetic field at \mathbf{r} is computed as

$$\mathbf{B} = \mathbf{C}_{\bar{B}} \mathbf{s}. \quad (3.25)$$

Quantities related to energy can be obtained using quadratic expressions: Using the inductance matrix \mathbf{M} (for definitions, see [166]), the quadratic expression $\mathbf{s}^\top \mathbf{M} \mathbf{s} / 2$ is the inductive field energy of the surface-current density. With the resistance matrix \mathbf{R} , the quadratic expression $\mathbf{s}^\top \mathbf{R} \mathbf{s}$ gives the Ohmic (heating) power of the surface current.

Surface harmonics

The most flexible choice of basis for the stream function on a triangle mesh is arguably the direct use of the hat function basis, in which the surface current around each mesh vertex is described independently. Alternatively, one can apply the eigenfunctions of the surface Laplacian [168, 169], which are also known as *surface harmonics* (SUH; Fig. 3.11; [166]).

The surface harmonics can be seen as a generalization of the more well-known spatial-frequency representations: on a sphere, the surface harmonics are essentially the spherical harmonics, and on a 2D plane, they correspond to a 2D Fourier series [168]. The series can represent smoothly varying functions with a fairly small number of components, allowing the series to be truncated at a low order. For example, a stream function defined by the values on the 2000 vertices of a mesh might be expressed to a sufficient accuracy by 100 coefficients of the SUH series. Due to this compression, one can increase the mesh resolution without increasing the number of degrees of freedom and the computational cost, e.g., in optimization tasks such as coil design. Truncating the SUH series also acts as an intuitive way to limit the maximum spatial frequency of the stream function and thereby in effect also its spatial gradient.

The surface harmonics are computed numerically using the generalized eigenvalue equation of the discretized surface-Laplacian operator \mathbf{L} [168, 169]

$$-\mathbf{L}\mathbf{V} = \mathbf{N}\mathbf{V}\mathbf{K}, \quad (3.26)$$

where \mathbf{N} is a mass matrix taking into account the piece-wise linear discretization of the mesh and $\mathbf{K} = \text{diag}(k_1^2 \dots k_{N_h}^2)$ contains the eigenvalues corresponding to the squared spatial frequencies of the $N_h \leq N_v$ surface harmonics, which are given by the columns of the basis matrix $\mathbf{V} \in \mathbb{R}^{N_v \times N_h}$.

The SUH representation \mathbf{a} of a stream function \mathbf{s} can be obtained using the basis matrix \mathbf{V} as $\mathbf{s} = \mathbf{V}\mathbf{a}$. Correspondingly, the magnetic field (Eq. 3.25) can be computed directly from \mathbf{a} :

$$\mathbf{B} = \mathbf{C}_{\bar{B}} \mathbf{s} = \mathbf{C}_{\bar{B}} \mathbf{V} \mathbf{a}. \quad (3.27)$$

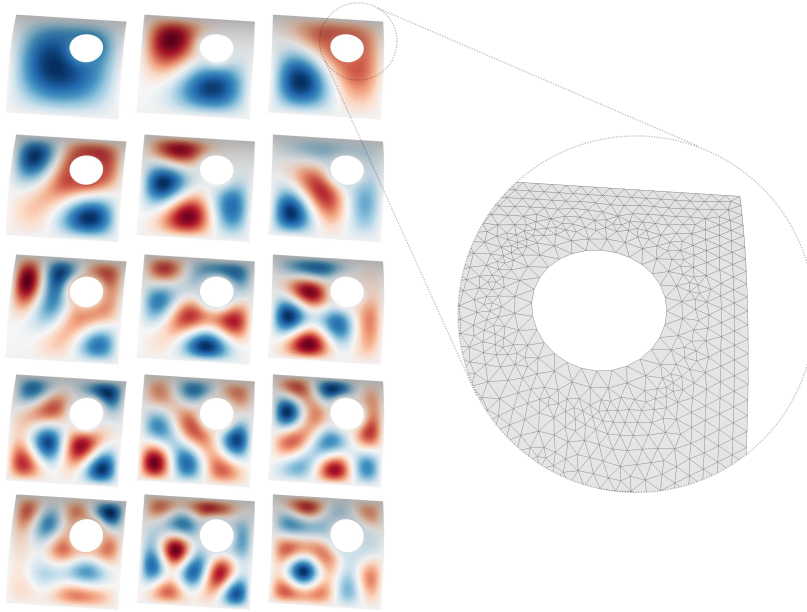


Figure 3.11. The first 15 surface harmonics of a triangle mesh representing a curved square with a hole. The index and thus spatial frequency increases from left to right, row by row. The tangential derivative is set to zero at the hole and outer boundaries. The mesh discretization is shown in the magnified inset on the right.

Thus, the SUH coefficients \mathbf{a} can be used to specify any field that can be produced by a surface current on the corresponding surface mesh.

Boundary conditions

For the stream function to represent a divergence-free surface current (without current flowing in or out of the mesh), the derivative of the stream function along the boundaries of the mesh must be zero. In other words, the stream function must be constant on the boundary. It is typically convenient to set its value on the outer boundary of the mesh to zero. When the mesh has inner boundaries, the stream function value for the vertices on each boundary should be equal (but not necessarily zero). To enforce this, the hat functions along an inner boundary are combined into a single basis function, the value of which is constant along the boundary.

3.5.2 Stream-function optimization and coil design

When designing surface coils in the stream-function framework, one must find an \mathbf{s} that fulfills the given requirements. This problem can be formulated as an optimization task. A requirement for minimal energy or power is convenient, since the optimization problem then becomes convex and thus has a unique solution which can be found efficiently. Other requirements for \mathbf{s} can be included

as inequality or equality constraints (e.g., one can constrain the magnetic field using Eq. 3.25), maintaining the convexity if the constraint equations are linear. A solution can be found as long as the set of constraints defines a non-empty set of candidate solutions.

Optimization methods

There are many alternative ways to formulate the (linearly constrained) quadratic optimization problem used in coil design. In a general form, the problem statement can be expressed as

$$\begin{aligned} &\text{minimize} && \frac{1}{2} \mathbf{s}^\top \mathbf{P} \mathbf{s} + \mathbf{q}^\top \mathbf{s} \\ &\text{subject to} && \mathbf{E} \mathbf{s} \leq \mathbf{f}, \\ &&& \mathbf{A} \mathbf{s} = \mathbf{b}, \end{aligned} \tag{3.28}$$

where \mathbf{P} is the quadratic objective matrix (e.g., inductance \mathbf{M} or resistance \mathbf{R}), \mathbf{q} defines an optional linear penalty term, and the linear equality and inequality constraints expressed using \mathbf{E} and \mathbf{A} are applied as needed. Multiple simultaneous constraints of the same type can easily be applied by stacking the constraint matrices. Furthermore, one may also include additional constraints, such as constraining the p -norm (e.g. 1-norm or ∞ -norm [170]) of a linear expression for \mathbf{s} $\|\mathbf{D}\mathbf{s} - \mathbf{t}\|_p \leq e$, or by constraining the stream function value of specific vertices to be equal: $\mathbf{s}_i = \mathbf{s}_j$. This problem can then be solved using an iterative numerical solver [171, 172] or, if no linear inequality constraints are used, using a least-squares approach with the addition of a trade-off parameter [158].

Objective functions

Typically, one of two different quadratic objectives are used in coil design: the minimization of the resistive power or the magnetic energy. Minimizing the resistive power $\mathbf{s}^\top \mathbf{R} \mathbf{s}$ results in a maximally smoothly varying stream function, as well as minimizing the resistive losses in the coil. This reduces the need for cooling the coil when large currents are used. Minimizing the magnetic energy $\mathbf{s}^\top \mathbf{M} \mathbf{s} / 2$ results in minimal inductance of the coil. This reduces the voltage required for fast ramping of the current in the coil.

Magnetic and resistive energy minimization typically result in fairly similar stream functions. The two functions differ in that magnetic energy minimization allows for somewhat more variation at higher spatial frequencies. These would be penalized more in resistive energy minimization. One may also form the quadratic objective as a weighted combination of resistive power and magnetic energy.

Constraints

Minimizing the quadratic objective without any penalty terms or linear constraints would lead to a trivial zero-current, zero-field solution. Thus, one must specify additional constraints to determine the final current pattern.

In coil design, constraining the magnetic field within a target region is the most typical constraint. In addition to specifying a target field one may also want to explicitly limit the stray field outside the coil. As presented in Publication IV, one can also place constraints on, e.g., the spherical harmonics representation of the magnetic field, on eddy-current-induced fields due to nearby conductors or even field distortion due to nearby magnetic shielding.

The use of inequality constraints in the optimization, as is possible when using an iterative solver, allows directly specifying the desired properties of the coil. This may be more intuitive than the use of trade-off/penalty parameters employed in the least-squares formulation. The use of inequality constraints also allows for wiggle room in the coil specification. This wiggle room decreases the need for *apodization* [157, 173], i.e. post-optimization smoothing of the stream function. Apodization has been applied due to high spatial-frequency oscillations or ‘ringing’ in the stream function, which can arise when a target-field equality constraint is used — especially when minimizing the magnetic energy.

More sophisticated methods to limit high-frequency ringing directly constrain the gradient of the stream function; the spatial gradient of the stream function defines the surface-current density, and by extension, the spacing of the discretized coil windings. Constraining the maximum gradient affects the minimum spacing of windings, which can also be useful with regard to manufacturability. Limiting the maximum current density can also decrease local heating issues in high-power applications. The minimax- $|j|$ method presented by [174, 175] is in effect a similar way to constrain the stream function gradient, but works somewhat differently from an optimization viewpoint. An alternative way to reduce the minimum spacing of windings is to use a truncated SUH basis limited to low spatial frequencies.

Discretization to wire segments and manufacturing

The continuous surface-current density is obtained from the optimized stream function with Eq. 3.24. To extract the geometry of discrete conductor loops, one can simply use any number of stream function isolines with equal spacing in terms of stream function value. The number of isolines, i.e. current loops, can be freely chosen to fit the application; more loops will obviously result in a larger magnetic field per unit current and larger inductance, but will also better approximate the continuous surface current, thus giving a smaller discretization error. Finally, the independent current loops must be connected in series, with special care taken to ensure that the current direction corresponds to the continuous current density. The manner in which the loops are connected should depend on manufacturing method and scale. For example, on a printed circuit board, the loops may be connected using vias and multiple layers, while larger-scale coils may use soldered wire segments. An example of a coil assembly manufactured using a printed circuit board (PCB) is shown in Fig. 3.12.

Manufacturability is a key issue for distributed winding coil designs. As the winding patterns can be complex, sophisticated manufacturing techniques may

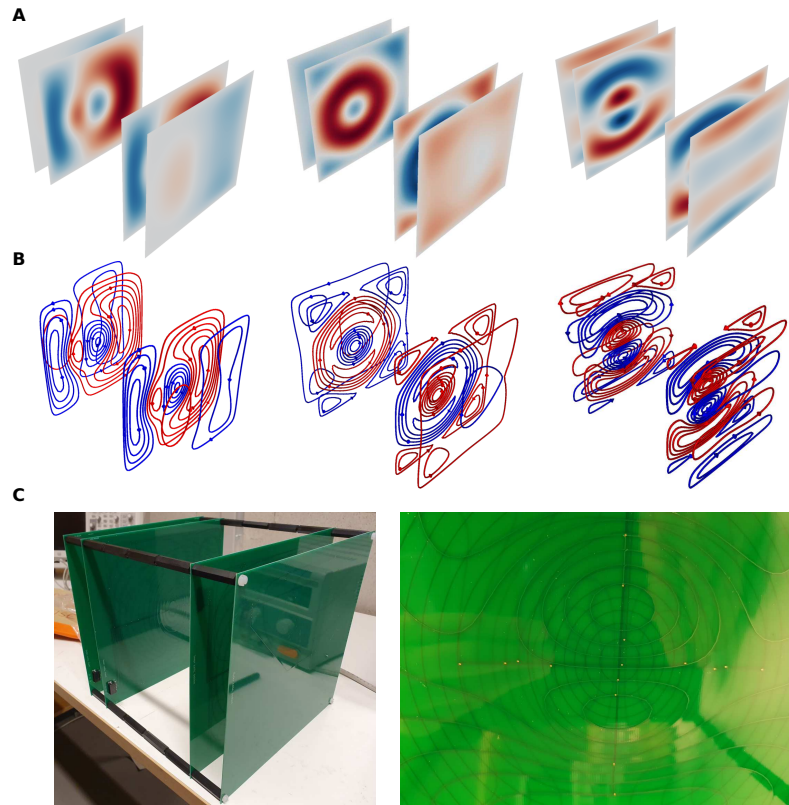


Figure 3.12. Design stages of a self-shielded planar coil assembly producing homogeneous field on all three axes. A: Optimized stream functions for all three axes. The homogeneous field volume is located between the coil planes, slightly offset on one axis. B: The resulting conductor windings. C: A manufactured coil prototype, including a close-up showing the implementation of the different coil windings on different PCB layers.

be needed to avoid errors in the geometry that lead to decreased performance. The manufacturing techniques applicable will depend on many factors such as the physical size of the coil, the geometry, the current amplitude, manufacturing scale (lab prototype or mass production), etc. Practical implementations for very small scales include different MEMS manufacturing techniques [176] and related microfabrication techniques. For small- to medium-scale planar coils, PCBs offer inexpensive, highly accurate and consistent manufacturing at any production volume. Using flexible PCBs, this capability can be extended to other geometries, e.g. by wrapping the flexible PCB around a cylinder [177]. For larger or more complex geometries, one may need to design a coil former onto which the conductor is wrapped. The former can be produced, e.g., using 3D-printing [178] or by machining [179].

3.5.3 Equivalent surface current models

The same stream-function framework used for coil design can also be used for interpolating the measured magnetic field in MEG at any point outside the head without requiring the use of a volume conductor model. In this method, we represent the measured magnetic field using an equivalent surface current density. We use the subject's scalp surface (extracted from an MR image) as the domain for the equivalent currents. Note that any surface that confines the “real” source currents generating the measured field would work. In order to determine the equivalent current distribution (corresponding to a stream function \mathbf{s}) that reconstruct the MEG measurements \mathbf{y} , we can apply a regularized least-squares method:

$$\begin{aligned} \text{minimize } E(\mathbf{s}) &= \mathbf{s}^\top (-\mathbf{L})\mathbf{s} + \lambda \|\mathbf{C}_{B_n}\mathbf{s} - \mathbf{y}\|^2 \\ &= \left(\mathbf{C}_{B_n}^\top \mathbf{C}_{B_n} + \frac{1}{\lambda} \mathbf{L} \right)^{-1} \mathbf{C}_{B_n}^\top \mathbf{y}, \end{aligned} \quad (3.29)$$

where the first term measures the norm of the current density over the surface with \mathbf{L} being the Laplacian operator (meaning that we assume the current density to be maximally smoothly varying), and the second term represents the residual between the measurements and the surface-current reconstruction. Here, \mathbf{C}_{B_n} is a coupling matrix that maps the stream function \mathbf{s} to the measured magnetic field component B_n at the sensor positions and λ is a trade-off parameter that balances between current smoothness and finding a current that accurately reconstructs \mathbf{y} . We can now use the stream function \mathbf{s} determined using Eq. 3.29 to compute the magnetic field at any point in the source-free space, as shown for an example MEG measurement in Fig. 3.13.

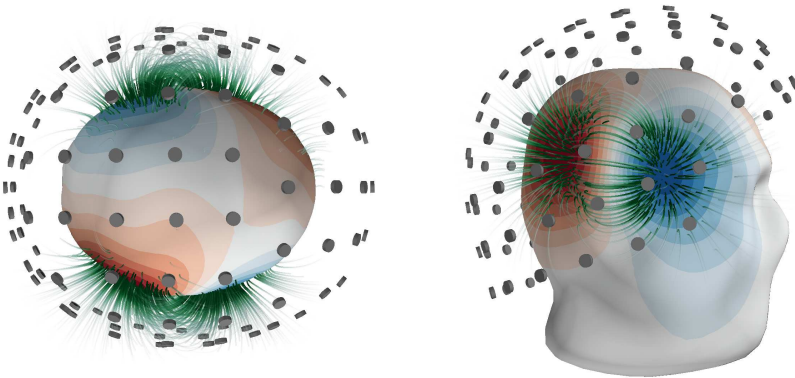


Figure 3.13. Equivalent surface current representation of an auditory evoked field measured with MEG, seen from top-down (left) and lateral views (right). The stream function on the subject's scalp surface is shown in red-blue colors, while the green stream lines represent the magnetic field reconstruction. The MEG sensors are shown as gray discs.

In the future, this method could be used in similar interference rejection

applications as SSS (see Section. 3.2.2), except with more general convergence properties [166]: instead of being limited to spherical shells, the method could be applied for any closed surface shapes.

4. Summary of Publications

4.1 Publication I: Requirements for Coregistration Accuracy in On-Scalp MEG

In this study, we aimed to find out how co-registration error affects on-scalp MEG measurements, and how accurate co-registration is required for good source modeling performance. At this point, the co-registration accuracy requirements of conventional SQUID-based MEG were well-studied, but how errors would affect source modeling when the sensors are directly placed on the scalp was unknown. We specifically considered on-scalp MEG systems in which each sensor is co-registered individually, such as for individually adaptable or even wearable sensor arrays.

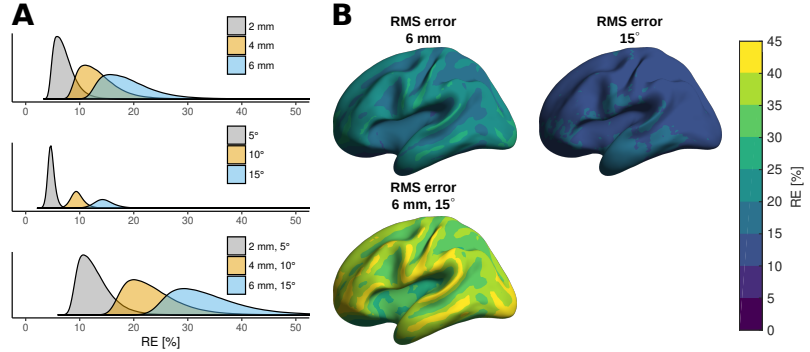


Figure 4.1. Relative error (RE) of on-scalp MEG sensor array topographies over all subjects at different levels of sensor position and orientation error. A: Error distributions shown as density plots. B: The mean RE over all subjects.

We used simulations to quantify how accurately one needs to know the position and orientation of sensors in such an on-scalp MEG system. We simulated a hypothetical whole-head on-scalp MEG sensor array which fit on 10 representative adult heads. The sensor array consisted of 184 sensors measuring the

field component normal to the scalp surface. The sensors had a scalp footprint of $20 \times 20 \text{ mm}^2$. From these reference sensor arrays, we constructed version with different amounts of co-registration error in the form of either random position or orientation error, or both. We then computed several error metrics (e.g. the relative error (RE) shown in Figure 4.1) for the forward model error due to the co-registration error. Further, we also studied the effect of the forward model error on source modeling using minimum-norm estimation, dipole fitting, and LCMV beamforming.

We found that sensor position errors generally have a larger effect than orientation errors and that these errors affect the localization accuracy of superficial sources the most. To obtain similar or higher accuracy than with current SQUID-based MEG systems, RMS sensor position and orientation errors should be $< 4 \text{ mm}$ and $< 10^\circ$, respectively.

4.2 Publication II: Optical co-registration of MRI and on-scalp MEG

The purpose of this study was to implement a co-registration method for on-scalp MEG fulfilling the requirements determined in Publication I while being fast and easy to use. We applied a consumer-grade structured-light scanner to create a surface mesh of the subject's head and the sensor array, which we fit to an MR image of the subject.

A summary of the developed co-registration procedure follows: after positioning the subject in the OPM-MEG system, an optical scan is performed by moving the structured-light scanner around the subject at a distance of approximately 50 cm. The digitized surface is visualized in real time, enabling the operator to perform quick corrections. The scan takes approximately 30 s to perform, depending on the desired coverage. The co-registration algorithm is initialized by a rough manual alignment of the optical scan mesh and the MR scalp mesh (Fig. 4.2, top panel). Since the optical scan includes both the subject's head and the MEG helmet with sensors, the area (vertices of the mesh) used for co-registration with the MR image should be limited. This is done by "painting" over the desired parts of the mesh with the computer mouse (Fig. 4.2, bottom-left panel). Being able to quickly constrain the areas used for co-registration makes it easy to exclude areas with visible artifacts. For co-registration of the MR scalp mesh and optical scan mesh, only the upper face and forehead areas are used, as other facial areas are more prone to movement or compression. After the initial alignment and vertex selection, the iterative closest point (ICP) algorithm with point-to-point minimization is run to automatically co-register the meshes. After co-registering the optical scan and the MR image, the same procedure is repeated to align the known geometry of the MEG helmet to the optical scan (transformed to MR coordinates).

We quantified the reproducibility of the optical scanning procedure and localized current dipoles using a head phantom. We found the scanner to fulfil

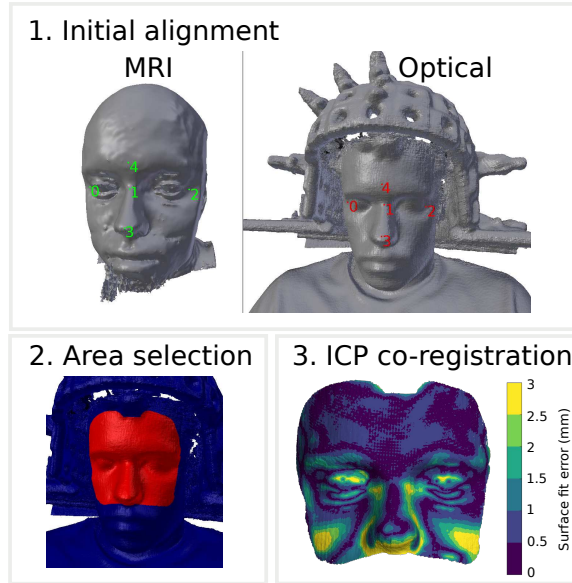


Figure 4.2. Optical co-registration procedure: 1. Initial mesh alignment with manually selected fiducial points, shown as coloured numerals, on the MR (left, green) and structured-light scan (right, red) meshes. Dummy sensors used to fix the head position are seen on either side of the head in the optical scan. 2. Selection of the co-registration area, selected area shown in red. 3. Automatic ICP-based co-registration and visualisation of the surface fit error.

our requirements, reproducing the head surface with <1 mm error between repetitions. Phantom dipoles were localized with 2.1 mm mean error.

Additionally, we measured somatosensory evoked fields (SEFs) to median nerve stimulation and compared the dipole positions between on-scalp and SQUID-based systems. SEF dipoles corresponding to the P35m response for OPMs were well localized to the somatosensory cortex, while SQUID dipoles for two subjects were erroneously localized to the motor cortex. The developed co-registration method is inexpensive, fast and can easily be applied to on-scalp MEG. It is more convenient than traditional co-registration methods while also being more accurate.

4.3 Publication III: Potential of on-scalp MEG: Robust detection of human visual gamma-band responses

In this study, we performed our first fully-fledged human OPM-MEG study. The main goal of this study was to demonstrate the performance of our on-scalp MEG system and compare it to a conventional SQUID-based MEG system. For our experimental paradigm, we used an attention-requiring task together with a dynamic visual stimulus known to elicit strong gamma-band responses in the visual cortical areas [20]. The measurement setup is shown in Fig. 4.3A.

Using an on-scalp array comprised of eight OPMs and a conventional 306-channel whole-head SQUID array, we performed MEG measurements for ten subjects. The measurements were carried out in a three-layer MSR without any additional active shielding. We applied the co-registration method developed in Publication II, and used DICS to model the cortical gamma-band source.

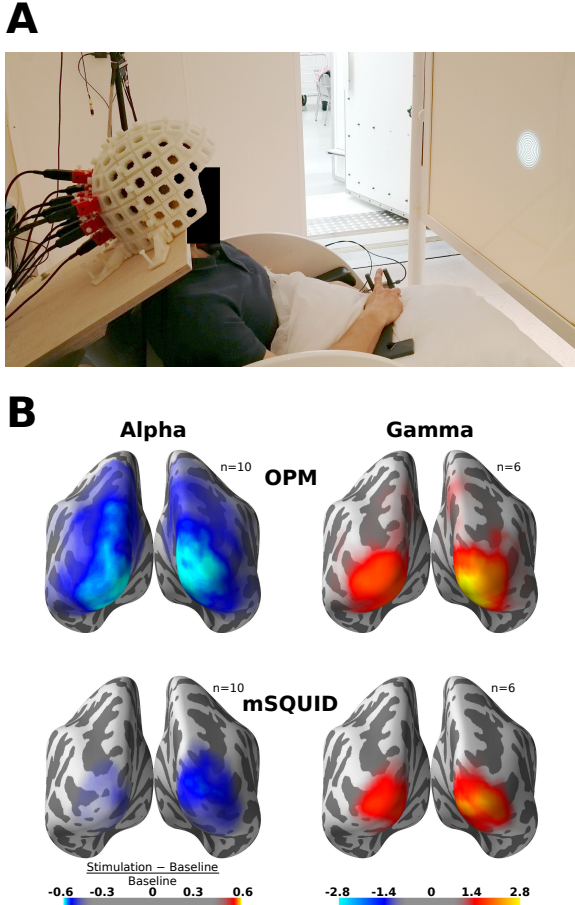


Figure 4.3. A: Experimental measurement setup inside the MSR. B: Grand-average source-power difference between visual stimulation and rest for alpha- and gamma-band activity for OPMs and SQUID magnetometers (mSQUID).

We found that the OPMs had substantially higher signal power than SQUIDs, and that they had a slightly larger relative gamma-power increase over the baseline. With only eight OPMs, we could obtain gamma-activity source estimates comparable to those of SQUIDs at the group level (see Fig. 4.3). Our results show the feasibility of using OPMs to measure gamma-band activity. To further facilitate the noninvasive detection of gamma-band activity, the on-scalp OPM arrays should be optimized with respect to sensor noise, the number of sensors and inter-sensor spacing.

4.4 Publication IV: Magnetic-field modeling with surface currents Part II: Implementation and usage of bfieldtools

OPM-based MEG requires the use of coils for field modulation, active magnetic shielding and negative feedback. In this study, we presented a novel open-source Python software package, `bfieldtools`, for magneto-quasistatic calculations with current densities on surfaces of arbitrary shape. The core functionality of the software relies on a stream-function representation of surface-current density and its discretization on a triangle mesh.

Although this stream-function technique is well-known in certain fields, to date the related software implementations have not been published or have been limited to specific applications. With `bfieldtools`, we aimed to produce a general, easy-to-use and well-documented open-source software. The software package is written purely in Python; instead of explicitly using lower-level languages, we address computational bottlenecks through extensive vectorization and use of the NumPy library. The package enables easy deployment, rapid code development and facilitates application of the software to practical problems. In this paper, we describe the software package and give an extensive demonstration of its use with an emphasis on one of its main applications – coil design. An example in which a biplanar coil that produces a homogeneous field in a target region between the two planes while producing minimal stray field around the coils is shown in Fig. 4.4.

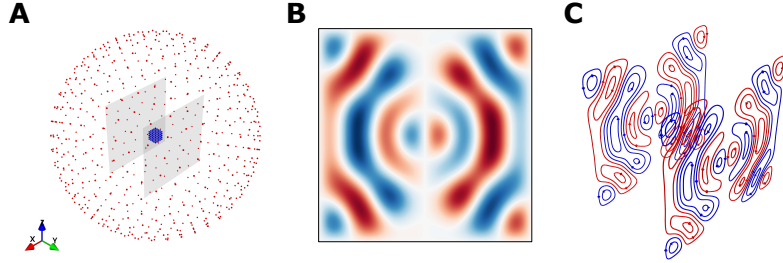


Figure 4.4. A: Biplanar coil surface meshes, target points (in blue) and stray field points (in red). B: Optimized stream function on one of the coil planes generating homogeneous magnetic field along the X-axis. C: Discretized coil windings.

5. Discussion

5.1 OPM-MEG system design

OPM-based MEG is not yet a mature imaging modality, and it remains to be seen how such MEG systems will look in the future. This section discusses different aspects of MEG instrumentation and system developments and the prospects of OPM-based MEG.

5.1.1 OPM sensor design

There is a myriad of ways one can construct OPMs, and the design choices can affect the entire OPM-MEG system design drastically. The OPM sensors themselves are not yet a mature technology, and constant developments are still taking place.

Until now, almost all OPM-MEG systems have used SERF OPMs due to their high sensitivity. While most SERF OPMs utilized for multi-channel OPM-MEG have been small individual-cell sensors using field modulation for readout [121, 138], there are also OPM-MEG systems using larger vapor cells with multiple readouts [128]. One possibility which shows promise [115, 120], but has not yet been fully exploited in OPM-MEG sensors is the ability to measure the full-vector magnetic field. It remains to be seen if the community will converge to a consensus regarding a specific design of SERF OPMs, or whether SERF OPMs will slowly be supplanted by other types of OPMs.

There are no fundamental reasons as to why other OPM types cannot reach similar sensitivity levels as current SERF OPMs. Recently, unshielded MEG measurements have been demonstrated using an OPM based on free-induction decay (FID) [180]. This type of magnetometer is elegant in its simplicity, as the Larmor frequency of a decaying spin polarization is simply directly read out using a frequency counter. FID-based OPMs can function in higher magnetic fields than SERF OPMs. The limiting factor is not the physics involved, but the upper limit of the frequency counter. Similarly, the sensor bandwidth is limited

by the FID sampling period. Another very recent publication [181] demonstrated a synchronous light-pulse atomic magnetometer (SLAM) in which SE collisions are suppressed even at ambient magnetic field strengths.

In contrast to SERF OPMs, both FID-based OPMs and SLAMs are intrinsically scalar magnetometers; they measure the field magnitude and are insensitive to its orientation (apart from some “dead zones” that depend on the readout strategy). Since there is typically a clearly dominant ambient field component, in practice this means that the sensitive axis is determined by the ambient field, and small field changes orthogonal to the dominant component are indiscernible.

Another promising way to improve OPM sensitivity, applicable to most OPM types, is to implement multipass cells [182], meaning that the laser light passes through the cell several times before reaching the readout photodiode. Multipass cells can be implemented by placing mirrors with precisely tuned shapes on either side of the cell [183], bouncing the light back and forth through the atomic medium for a specified number of times. This increase in optical depth leads, in simple terms, to more atom-light interaction and increased sensitivity.

Finally, there is the matter of gradiometers versus magnetometers: gradiometers are commonly applied in SQUID-MEG due to their attractive interference rejection properties and the fact that they are easily manufactured using SFTs. For OPMs, the construction of gradiometers is a more nuanced matter; one can simply use two magnetometers and subtract their signal, creating a *synthetic* gradiometer. However, this setup has no performance benefits and does not add any information to the measurement. A performance benefit can be achieved by using a single pump laser [177] and/or vapor cell [124] for the two magnetometer parts, thus removing technical common-mode noise from the pump laser and calibration issues due to small differences in cell pressure, etc. Finally, it is possible to create *intrinsic* OPM gradiometers that directly measure the magnetic field gradient [184]. It still remains to be seen which of these options will be the most attractive option for OPM-MEG.

5.1.2 Shielding

As discussed earlier, some OPM types may not require any shielding, but can operate in the ambient geomagnetic field. However, the fact that the sensors work does not mean that one can measure MEG signals in typical unshielded environments; interference due to power lines, moving vehicles, etc. will drown out any MEG signal. The first demonstration of unshielded OPM-MEG measurements was performed using a FID-based OPM gradiometer away from urban interference sources [180]. Similarly, some of the earliest SQUID-based MEG measurements in Finland were carried out in a wooden hut on top of a frozen lake, far away from electrical power lines and other urban interference sources (the main reason for the unshielded measurements was simply to avoid the expense of an MSR) [185]. While these MEG measurements are possible in magnetically clean environments, this may not translate to more urban environ-

ments such as university campuses and hospitals. Shielding will probably still be required, but it is conceivable that significantly less shielding than currently is used may suffice, especially when using gradiometers.

For SERF-based systems that require a low background field, substantial shielding will still be required. While many current SQUID-based MEG systems use very bulky and expensive MSRs, smaller OPM-based MEG systems may be able to utilize lighter-weight and more compact shields, which would then be complemented by active shielding.

5.1.3 Wearable MEG

Since OPMs do not require bulky cryogenics and can be significantly miniaturized, there has been considerable interest in creating wearable OPM-MEG systems in which the subject is free to move their head or even walk around inside an MSR [96]. Wearable MEG would open up new paradigms and use-cases. These include, e.g., easier measurements of subjects who are unable to remain still, such as young children and certain patient groups, as well as neuroscientific experiments investigating motor control in which subjects can move naturally [139].

Wearable systems and moving subjects will pose additional challenges in terms of shielding, especially with SERF OPMs. The remanent ambient field within MSRs is several orders of magnitude larger than the MEG signal. Even if the remanent field can be canceled at the sensor locations, nulling the entire ambient field within a larger volume to the same order of magnitude as the MEG signal would be extremely challenging. The large movement artifacts due to sensor movements within an ambient field will cause sensor calibration errors (see Section 3.4.1). Thus, wearable MEG systems will need good cancellation of the remanent field as well as sensors operating using negative feedback to keep the calibration stable. Using software methods to cancel out movement artifacts based on motion tracking [140] can reduce the artifact to a fraction of the original amplitude but will not account for the calibration error.

5.1.4 Co-registration

Co-registration instrumentation is an essential part of MEG systems, and with the arrival of OPM-based MEG there has been a variety of new co-registration methods used. Ideally, one would want a ‘built-in’ co-registration method that provides accurate results as well as real-time motion tracking without any additional manual work or equipment.

Optical 3D scanning methods in which the surface of the subject’s head is mapped, such as the one developed in Publication II can provide accurate results but do require some manual work. Implementing continuous tracking with such scanners is possible but would be computationally heavy and require offline reconstruction. A strategy in which the initial co-registration is performed using

a 3D scanner and subsequently, real-time tracking is performed by tracking reflective or colored markers (as in e.g. [139]) would be preferable. Ideally, the same scanning device could be used for both co-registration stages.

Optical methods have some issues, the most obvious one being that they require line-of-sight. All co-registration methods relying on digitizing the outer casing of the sensors will have some error; depending on the sensor manufacturing methods, there may be some degree of uncertainty on the exact location of the sensitive volume. More importantly, if the field is not exactly zero, or if there is crosstalk between the sensors, the sensitive axis of SERF OPMs may not be aligned with its casing. Using the sensor response to some signal that can be modeled in a known coordinate system, one can electromagnetically localize the *effective* sensor, not simply the sensor casing. Electromagnetic co-registration could be implemented using a somewhat large number of small coils with known field profiles and locations [97, 98], or alternatively using a set of large coils and gradient encoding somewhat similar to what used in MRI. These methods can also be used to provide real-time tracking, e.g. using sinusoidal signals and lock-in detection, which would then consume sensor bandwidth. This may be an issue, especially for SERF OPMs with small bandwidths.

5.1.5 Sampling

Generally, one wishes to measure the magnetic field over the entire scalp. The question is then how many sensors one needs to cover the scalp, and how should they be placed in order to sufficiently sample the neuromagnetic field [39].

A crucial part of the sampling problem relates to what components of the magnetic field is measured. Conventional SQUID-based MEG systems typically measure the magnetic field component normal to the scalp surface, and most OPM-based MEG systems do the same. It has been shown that, out of any single field component, this component provides the most information about cortical activity [102]. However, if one can measure the full vector magnetic field instead of a single field component, this changes the sampling problem; perhaps one could use a smaller number of full-vector magnetometers instead of a dense array of single-component magnetometers. A hybrid system in which a mixed array of lower-noise single-axis sensors are complemented by higher-noise full-vector sensors is also an option. The sampling problem is again flipped on its head if all sensors would measure the same field component, as is the *de facto* case with scalar magnetometers in a large ambient field.

Another interesting proposition is to produce flexible, application-specific OPM-MEG systems with a smaller number of sensors. These sensors would then be placed around cortical regions of interest instead of uniformly covering the entire scalp. This type of system could e.g. be applied for clinical use when mapping the sensorimotor system, or for noninvasive brain-computer interfaces (BCIs) [186, 187].

5.2 Coil design & stream functions

The stream-function-based framework for magnetic field modeling and surface coil design presented in Publication IV and its sister article by Mäkinen et al. [166] has been well-known in some fields of science and specific communities (as listed in Sec. 3.5.1). However, the implementations described in the literature have typically not been openly shared. With the easy access provided by the release of the open-source `bfieldtools` software package, the framework will hopefully be more broadly adopted across different fields of science and engineering. In this section, some MEG-specific example applications of the stream-function modeling framework are outlined.

5.2.1 Active shielding

As there is a general desire to move towards lighter shielding, person-sized shield and even wearable MEG, active shielding is becoming essential. For MSR-type shields, stream-function-based coil design may enable shielding systems that leave easy access to the subject, or coils allowing for wearable or even ambulatory MEG. Such coils have already been developed and have proven themselves to allow wearable MEG in conjunction with additional software interference rejection [140, 188].

In compact person-sized shields, one may design coils that efficiently fit the shield geometry while still having good performance. In addition, by modeling the magnetic shielding as in Publication IV, one can prospectively take the distorting effect of the passive shielding into account when designing the coil.

5.2.2 OPM design

A direct application of stream-function-based coil design for OPM-based MEG is in the design of (SERF) OPMs suitable for use in dense arrays. When the sensors are close to each other, it is important that their field nulling coils don't produce a large stray field, as any vibrations or relative movement of sensors is then seen as artifacts in neighboring sensors. Additionally, if the sensors utilize field modulation in the signal readout, the stray field may introduce crosstalk by tilting the sensitive axis of the neighboring sensors.

Coil designs that minimize crosstalk have already [189, 190] been developed. These designs have utilized simple, individual current loops on two cylindrical shells, creating a self-shielding coil that produces a homogeneous field along the cylinder axis. In these designs, the other two field components were produced by saddle coils, which were not self-shielded. The use of stream-function-based methods would allow for more complex winding patterns, which in turn could enable the use of simpler coil assemblies and easier-to-manufacture designs while also enabling the design of self-shielded coils for all three axes (see Fig. 3.12 for an example).

In addition to coils, miniature OPM sensors require conductive components such as resistive heaters and mirrors placed in close proximity to the vapor cell. By computing the thermal noise caused by these conductive components in the design stage [148], one can ensure that the performance of the sensor is not limited by thermal noise issues inherent to the sensor.

5.3 Prospects of on-scalp MEG

At the time of writing, it seems like on-scalp MEG based on OPMs has reached the point of critical mass. There is now considerable commercial interest in this field, with new companies being formed in several countries. We are bound to see the launch of several commercial systems in the coming 5–10 years, followed by a “weeding out” of companies who cannot compete or otherwise survive financially. This same pattern occurred for SQUID-based MEG in the 1990s: there was a boom of new MEG companies and products. Then, as the MEG market did not see the large expansion that investors hoped for, a number of bankruptcies, takeovers and other actions governed as much by the business side as by the technical merit of the products followed.

While on-scalp MEG offers many advantages over SQUID-based MEG (as listed in this Thesis), no new “killer application” has yet been demonstrated. Herein lies a tricky issue: in order to empirically and fully demonstrate the advantages of on-scalp MEG, a whole-head coverage system with dense sampling needs to be built. To build such a system requires funds, time and the solving of several engineering challenges. Nevertheless, if e.g. such a system could (even partially) replace invasive measurements, it would revolutionize the field of neuroimaging.

If no new “killer application” materializes, MEG will probably remain somewhat of a niche method despite the advantages of on-scalp MEG. Hopefully, this niche will still grow as performance goes up and costs come down. In this case, on-scalp MEG will probably replace the current SQUID-based MEG systems in some use-cases and complement them in others. This will happen quicker in research applications than in clinical use due to regulatory approval processes slowing things down. Along the way, MEG will continue to be applied to important neuroscientific questions, gaining us valuable insights into the working of the brain, our most complex organ.

References

- [1] Y. Tang, J. R. Nyengaard, D. M. G. D. Groot, and H. J. G. Gundersen. “Total Regional and Global Number of Synapses in the Human Brain Neocortex”. *Synapse* 41.3 (2001), pp. 258–273.
- [2] F. A. C. Azevedo, L. R. B. Carvalho, L. T. Grinberg, J. M. Farfel, R. E. L. Ferretti, R. E. P. Leite, W. J. Filho, R. Lent, and S. Herculano-Houzel. “Equal Numbers of Neuronal and Nonneuronal Cells Make the Human Brain an Isometrically Scaled-up Primate Brain”. *Journal of Comparative Neurology* 513.5 (2009), pp. 532–541.
- [3] T. M. McKenna, J. L. Davis, and S. F. Zornetzer. *Single Neuron Computation*. Academic Press, 2014. 663 pp.
- [4] R. Srinivasan, D. M. Tucker, and M. Murias. “Estimating the Spatial Nyquist of the Human EEG”. *Behavior Research Methods, Instruments, & Computers* 30.1 (1998), pp. 8–19.
- [5] M. S. Hämmäläinen, R. Hari, R. J. Ilmoniemi, J. Knuutila, and O. V. Lounasmaa. “Magnetoencephalography - Theory, Instrumentation, and Applications to Noninvasive Studies of the Working Human Brain”. *Reviews of Modern Physics* 65.2 (1993), pp. 413–505.
- [6] R. Hari and R. Salmelin. “Magnetoencephalography: From SQUIDS to Neuroscience. Neuroimage 20th Anniversary Special Edition.” *NeuroImage* 61.2 (2012), pp. 386–396.
- [7] S. Baillet. “Magnetoencephalography for Brain Electrophysiology and Imaging”. *Nature Neuroscience* 20.3 (2017), pp. 327–339.
- [8] S. Kharkar and R. Knowlton. “Magnetoencephalography in the Presurgical Evaluation of Epilepsy”. *Epilepsy & Behavior* 46 (2015), pp. 19–26.
- [9] J. P. Mäkelä, N. Forss, J. Jääskeläinen, E. Kirveskari, A. Korvenoja, and R. Paetau. “Magnetoencephalography in Neurosurgery”. *Neurosurgery* 59.3 (2006), pp. 493–511.

- [10] P. E. Tarapore, M. C. Tate, A. M. Findlay, S. M. Honma, D. Mizuiri, M. S. Berger, and S. S. Nagarajan. “Preoperative Multimodal Motor Mapping: A Comparison of Magnetoencephalography Imaging, Navigated Transcranial Magnetic Stimulation, and Direct Cortical Stimulation”. *Journal of Neurosurgery* 117.2 (2012), pp. 354–362.
- [11] J. D. Lewine, J. T. Davis, E. D. Bigler, R. Thoma, D. Hill, M. Funke, J. H. Sloan, S. Hall, and W. W. Orrison. “Objective Documentation of Traumatic Brain Injury Subsequent to Mild Head Trauma: Multimodal Brain Imaging With MEG, SPECT, and MRI”. *The Journal of Head Trauma Rehabilitation* 22.3 (2007), pp. 141–155.
- [12] M. Huang, M. Risling, and D. G. Baker. “The Role of Biomarkers and MEG-Based Imaging Markers in the Diagnosis of Post-Traumatic Stress Disorder and Blast-Induced Mild Traumatic Brain Injury”. *Psychoneuroendocrinology* 63 (2016), pp. 398–409.
- [13] D. Budker and M. Romalis. “Optical Magnetometry”. *Nature Physics* 3.4 (2007), pp. 227–234.
- [14] S. Murakami and Y. Okada. “Contributions of Principal Neocortical Neurons to Magnetoencephalography and Electroencephalography Signals”. *The Journal of Physiology* 575.3 (2006), pp. 925–936.
- [15] S. Ramón y Cajal. *Comparative Study of the Sensory Areas of the Human Cortex*. 1889.
- [16] M. Haller, T. Donoghue, E. Peterson, P. Varma, P. Sebastian, R. Gao, T. Noto, R. T. Knight, A. Shestyuk, and B. Voytek. “Parameterizing Neural Power Spectra”. *bioRxiv* (2018), p. 299859.
- [17] J. J. Newson and T. C. Thiagarajan. “EEG Frequency Bands in Psychiatric Disorders: A Review of Resting State Studies”. *Frontiers in Human Neuroscience* 12 (2019).
- [18] G. Curio. “Linking 600-Hz “Spikelike” EEG/MEG Wavelets (“ ζ -Bursts”) to Cellular Substrates: Concepts and Caveats”. *Journal of Clinical Neurophysiology* 17.4 (2000), pp. 377–396.
- [19] G. Buzsaki. *Rhythms of the Brain*. Oxford University Press, 2011. 448 pp.
- [20] N. Hoogenboom, J. M. Schoffelen, R. Oostenveld, L. M. Parkes, and P. Fries. “Localizing Human Visual Gamma-Band Activity in Frequency, Time and Space”. *NeuroImage* 29.3 (2006), pp. 764–773.
- [21] X.-J. Wang. “Neurophysiological and Computational Principles of Cortical Rhythms in Cognition”. *Physiological Reviews* 90.3 (2010), pp. 1195–1268.
- [22] O. Jensen and A. Mazaheri. “Shaping Functional Architecture by Oscillatory Alpha Activity: Gating by Inhibition”. *Frontiers in Human Neuroscience* 4 (2010).

- [23] T. H. Donner and M. Siegel. “A Framework for Local Cortical Oscillation Patterns”. *Trends in Cognitive Sciences* 15.5 (2011), pp. 191–199.
- [24] P. Fries. “Rhythms for Cognition: Communication through Coherence”. *Neuron* 88.1 (2015), pp. 220–235.
- [25] S. R. Cole and B. Voytek. “Brain Oscillations and the Importance of Waveform Shape”. *Trends in Cognitive Sciences* 21.2 (2017), pp. 137–149.
- [26] N. E. Crone, A. Korzeniewska, and P. J. Franaszczuk. “Cortical Gamma Responses: Searching High and Low”. *International Journal of Psychophysiology* 79.1 (2011), pp. 9–15.
- [27] J. P. Lachaux, N. Axmacher, F. Mormann, E. Halgren, and N. E. Crone. “High-Frequency Neural Activity and Human Cognition: Past, Present and Possible Future of Intracranial EEG Research”. *Progress in Neurobiology* 98.3 (2012), pp. 279–301.
- [28] J. Liu and W. T. Newsome. “Local Field Potential in Cortical Area MT: Stimulus Tuning and Behavioral Correlations”. *Journal of Neuroscience* 26.30 (2006), pp. 7779–7790.
- [29] S. Ray, N. E. Crone, E. Niebur, P. J. Franaszczuk, and S. S. Hsiao. “Neural Correlates of High-Gamma Oscillations (60–200 Hz) in Macaque Local Field Potentials and Their Potential Implications in Electrocorticography”. *Journal of Neuroscience* 28.45 (2008), pp. 11526–11536.
- [30] A. Belitski, A. Gretton, C. Magri, Y. Murayama, M. A. Montemurro, N. K. Logothetis, and S. Panzeri. “Low-Frequency Local Field Potentials and Spikes in Primary Visual Cortex Convey Independent Visual Information”. *Journal of Neuroscience* 28.22 (2008), pp. 5696–5709.
- [31] K. J. Miller, C. J. Honey, D. Hermes, R. P. Rao, J. G. Ojemann, et al. “Broadband Changes in the Cortical Surface Potential Track Activation of Functionally Diverse Neuronal Populations”. *NeuroImage* 85 (2014), pp. 711–720.
- [32] M. C. Cervenka, P. J. Franaszczuk, N. E. Crone, B. Hong, B. S. Caffo, P. Bhatt, F. A. Lenz, and D. Boatman-Reich. “Reliability of Early Cortical Auditory Gamma-Band Responses”. *Clinical Neurophysiology* 124.1 (2013), pp. 70–82.
- [33] D. Hermes, K. J. Miller, B. A. Wandell, and J. Winawer. “Stimulus Dependence of Gamma Oscillations in Human Visual Cortex”. *Cerebral Cortex* 25.9 (2015), pp. 2951–2959.
- [34] E. Bartoli, W. Bosking, Y. Chen, Y. Li, S. A. Sheth, M. S. Beauchamp, D. Yoshor, and B. L. Foster. “Functionally Distinct Gamma Range Activity Revealed by Stimulus Tuning in Human Visual Cortex”. *Current Biology* 29 (2019), pp. 3345–3358.

- [35] F. de Pasquale, S. D. Penna, A. Z. Snyder, C. Lewis, D. Mantini, L. Marzetti, P. Belardinelli, L. Ciancetta, V. Pizzella, G. L. Romani, and M. Corbetta. “Temporal Dynamics of Spontaneous MEG Activity in Brain Networks”. *Proceedings of the National Academy of Sciences* 107.13 (2010), pp. 6040–6045.
- [36] D. Cohen. “Magnetoencephalography: Evidence of Magnetic Fields Produced by Alpha-Rhythm Currents.” *Science* 161.843 (1968), pp. 784–786.
- [37] R. C. Jaklevic, J. Lambe, A. H. Silver, and J. E. Mercereau. “Quantum Interference Effects in Josephson Tunneling”. *Physical Review Letters* 12.7 (1964), pp. 159–160.
- [38] D. Cohen. “Magnetoencephalography: Detection of the Brain’s Electrical Activity with a Superconducting Magnetometer”. *Science* 175.4022 (1972), pp. 664–666.
- [39] J. Iivanainen, A. J. Mäkinen, R. Zetter, M. Stenroos, R. J. Ilmoniemi, and L. Parkkonen. “Spatial Sampling of MEG and EEG Revisited: From Spatial-Frequency Spectra to Model-Informed Sampling”. *arXiv* (2020), p. 2006.02919.
- [40] A. I. Ahonen, M. S. Hämäläinen, R. J. Ilmoniemi, M. J. Kajola, J. E. Knuutila, J. T. Simola, and V. A. Vilkman. “Sampling Theory for Neuromagnetic Detector Arrays”. *IEEE Transactions on Biomedical Engineering* 40.0 (1993), pp. 859–869.
- [41] L. Parkkonen. “Instrumentation and Data Preprocessing”. In: *MEG: An Introduction to Methods*. Ed. by P. Hansen, M. Kringelbach, and R. Salmelin. Oxford University Press, 2010, pp. 24–64.
- [42] Y.-H. Lee and K. Kim. “Instrumentation for Measuring MEG Signals”. In: *Magnetoencephalography*. Ed. by S. Supek and C. J. Aine. Berlin, Heidelberg: Springer Berlin Heidelberg, 2014, pp. 3–33.
- [43] A. Borna, T. R. Carter, A. P. Colombo, Y.-Y. Jau, J. McKay, M. Weisend, S. Taulu, J. M. Stephen, and P. D. D. Schwindt. “Non-Invasive Functional Brain-Imaging with an OPM-Based Magnetoencephalography System”. *PLOS ONE* 15.1 (2020), e0227684.
- [44] K. He, S. Wan, J. Sheng, D. Liu, C. Wang, D. Li, L. Qin, S. Luo, J. Qin, and J.-H. Gao. “A High-Performance Compact Magnetic Shield for Optically Pumped Magnetometer-Based Magnetoencephalography”. *Review of Scientific Instruments* 90.6 (2019), p. 064102.
- [45] X. De Tiège, M. O. de Beeck, M. Funke, B. Legros, L. Parkkonen, S. Goldman, and P. Van Bogaert. “Recording Epileptic Activity with MEG in a Light-Weight Magnetic Shield”. *Epilepsy Research* 82.2 (2008), pp. 227–231.

- [46] Y. Okada et al. “BabyMEG: A Whole-Head Pediatric Magnetoencephalography System for Human Brain Development Research”. *Review of Scientific Instruments* 87.9 (2016), p. 094301.
- [47] E. Carrette, M. Op De Beeck, M. Bourguignon, P. Boon, K. Vonck, B. Legros, S. Goldman, P. Van Bogaert, and X. De Tiege. “Recording Temporal Lobe Epileptic Activity with MEG in a Light-Weight Magnetic Shield”. *Seizure* 20.5 (2011), pp. 414–418.
- [48] M. A. Uusitalo and R. J. Ilmoniemi. “Signal-Space Projection Method for Separating MEG or EEG into Components”. *Medical and Biological Engineering and Computing* 35.2 (1997), pp. 135–140.
- [49] S. Taulu, M. Kajola, and J. Simola. “Suppression of Interference and Artifacts by the Signal Space Separation Method”. *Brain Topography* 16.4 (2004), pp. 269–275.
- [50] S. Taulu and J. Simola. “Spatiotemporal Signal Space Separation Method for Rejecting Nearby Interference in MEG Measurements”. *Physics in Medicine and Biology* 51.7 (2006), pp. 1759–1768.
- [51] R. Vigário, V. Jousmäki, M. Hämäläinen, R. Hari, and E. Oja. “Independent Component Analysis for Identification of Artifacts in Magnetoencephalographic Recordings”. In: *Advances in Neural Information Processing Systems 10*. MIT Press, 1998, pp. 229–235.
- [52] C. A. Brebbia, J. C. F. Telles, and L. Wrobel. *Boundary Element Techniques: Theory and Applications in Engineering*. Springer Science & Business Media, 2012.
- [53] B. A. Szabo and I. Babuška. *Finite Element Analysis*. John Wiley & Sons, 1991.
- [54] A. Thielscher, A. Antunes, and G. B. Saturnino. “Field Modeling for Transcranial Magnetic Stimulation: A Useful Tool to Understand the Physiological Effects of TMS?” In: *2015 37th Annual International Conference of the IEEE Engineering in Medicine and Biology Society (EMBC)*. 2015, pp. 222–225.
- [55] D. B. Geselowitz. “On the Magnetic Field Generated Outside an Inhomogeneous Volume Conductor by Internal Current Sources”. *IEEE Transactions on Magnetics* 6.2 (1970), pp. 346–347.
- [56] A. S. Ferguson and G. Stroink. “Factors Affecting the Accuracy of the Boundary Element Method in the Forward Problem-I: Calculating Surface Potentials”. *IEEE Transactions on Biomedical Engineering* 44.11 (1997), pp. 1139–1155.
- [57] M. Stenroos, A. Hunold, and J. Hauelsen. “Comparison of Three-Shell and Simplified Volume Conductor Models in Magnetoencephalography”. *NeuroImage* 94 (2014), pp. 337–348.

- [58] J. Sarvas. “Basic Mathematical and Electromagnetic Concepts of the Biomagnetic Inverse Problem.” *Physics in Medicine and Biology* 32.1 (1987), pp. 11–22.
- [59] T. F. Oostendorp, J. Delbeke, and D. F. Stegeman. “The Conductivity of the Human Skull: Results of in Vivo and in Vitro Measurements”. *IEEE Transactions on Biomedical Engineering* 47.11 (2000), pp. 1487–1492.
- [60] M. Akhtari et al. “Conductivities of Three-Layer Live Human Skull.” *Brain Topography* 14.3 (2002), pp. 151–167.
- [61] Y. Lai, W. Van Drongelen, L. Ding, K. E. Hecox, V. L. Towle, D. M. Frim, and B. He. “Estimation of in Vivo Human Brain-to-Skull Conductivity Ratio from Simultaneous Extra- and Intra-Cranial Electrical Potential Recordings”. *Clinical Neurophysiology* 116.2 (2005), pp. 456–465.
- [62] Y. Zhang, W. Van Drongelen, and B. He. “Estimation of in Vivo Brain-to-Skull Conductivity Ratio in Humans”. *Applied Physics Letters* 89 (2006), p. 223903.
- [63] M. Dannhauer, B. Lanfer, C. H. Wolters, and T. R. Knösche. “Modeling of the Human Skull in EEG Source Analysis”. *Human Brain Mapping* 32.9 (2011), pp. 1383–1399.
- [64] M. Stenroos and O. Hauk. “Minimum-Norm Cortical Source Estimation in Layered Head Models Is Robust against Skull Conductivity Error”. *NeuroImage* 81 (2013), pp. 265–272.
- [65] M. Stenroos and A. Nummenmaa. “Incorporating and Compensating Cerebrospinal Fluid in Surface-Based Forward Models of Magneto- and Electroencephalography”. *PLOS ONE* 11.7 (2016), e0159595.
- [66] J. Mosher, S. Baillet, and R. Leahy. “Equivalence of Linear Approaches in Bioelectromagnetic Inverse Solutions”. In: *IEEE Workshop on Statistical Signal Processing, 2003*. 2003, pp. 294–297.
- [67] M. S. Hämäläinen and R. J. Ilmoniemi. “Interpreting Magnetic Fields of the Brain: Minimum Norm Estimates”. *Medical & Biological Engineering & Computing* 32.1 (1994), pp. 35–42.
- [68] O. Hauk. “Keep It Simple: A Case for Using Classical Minimum Norm Estimation in the Analysis of EEG and MEG Data”. *NeuroImage* 21.4 (2004), pp. 1612–1621.
- [69] F. H. Lin, T. Witzel, S. P. Ahlfors, S. M. Stufflebeam, J. W. Belliveau, and M. S. Hämäläinen. “Assessing and Improving the Spatial Accuracy in MEG Source Localization by Depth-Weighted Minimum-Norm Estimates”. *NeuroImage* 31.1 (2006), pp. 160–171.
- [70] A. M. Dale, A. K. Liu, B. R. Fischl, R. L. Buckner, J. W. Belliveau, J. D. Lewine, and E. Halgren. “Dynamic Statistical Parametric Mapping”. *Neuron* 26.1 (2000), pp. 55–67.

- [71] R. D. Pascual-Marqui. “Standardized Low Resolution Brain Electromagnetic Tomography (sLORETA): Technical Details”. *Methods & Findings in Experimental & Clinical Pharmacology* (2002).
- [72] B. Van Veen, W. van Drongelen, M. Yuchtman, and A. Suzuki. “Localization of Brain Electrical Activity via Linearly Constrained Minimum Variance Spatial Filtering”. *IEEE Transactions on Biomedical Engineering* 44.9 (1997), pp. 867–880.
- [73] M. X. Huang, J. J. Shih, R. R. Lee, D. L. Harrington, R. J. Thoma, M. P. Weisend, F. Hanlon, K. M. Paulson, T. Li, K. Martin, G. A. Miller, and J. M. Canive. “Commonalities and Differences among Vectorized Beamformers in Electromagnetic Source Imaging”. *Brain Topography* 16.3 (2004), pp. 139–158.
- [74] A. Hillebrand and G. R. Barnes. “Beamformer Analysis of MEG Data”. *International Review of Neurobiology* 68.05 (2005), pp. 149–171.
- [75] K. Sekihara, S. S. Nagarajan, D. Poeppel, and A. Marantz. “Performance of an MEG Adaptive-Beamformer Source Reconstruction Technique in the Presence of Additive Low-Rank Interference”. *IEEE Transactions on Biomedical Engineering* 51.1 (2004), pp. 90–99.
- [76] J. Vrba, S. Taulu, J. Nenonen, and A. Ahonen. “Signal Space Separation Beamformer”. *Brain Topography* 23.2 (2010), pp. 128–133.
- [77] J. Gross, J. Kujala, M. Hämäläinen, L. Timmermann, A. Schnitzler, and R. Salmelin. “Dynamic Imaging of Coherent Sources: Studying Neural Interactions in the Human Brain”. *Proceedings of the National Academy of Sciences* 98.2 (2001), pp. 694–699.
- [78] R. Salmelin. “Multi-Dipole Modeling in MEG”. In: *MEG: An Introduction to Methods*. Ed. by P. Hansen, M. Kringelbach, and R. Salmelin. Oxford University Press, 2010.
- [79] N. Hironaga, K. Hagiwara, K. Ogata, M. Hayamizu, T. Urakawa, and S. Tobimatsu. “Proposal for a New MEG–MRI Co-Registration: A 3D Laser Scanner System”. *Clinical Neurophysiology* 125.12 (2014), pp. 2404–2412.
- [80] P. Adjarian, G. R. Barnes, A. Hillebrand, I. E. Holliday, K. D. Singh, P. L. Furlong, E. Harrington, C. W. Barclay, and P. J. G. Route. “Co-Registration of Magnetoencephalography with Magnetic Resonance Imaging Using Bite-Bar-Based Fiducials and Surface-Matching”. *Clinical Neurophysiology* 115.3 (2004), pp. 691–698.
- [81] H. Sonntag, J. Haueisen, and B. Maes. “Quality Assessment of MEG-to-MRI Coregistrations”. *Physics in Medicine and Biology* 63 (2018), p. 075003.

- [82] F. Chella, L. Marzetti, M. Stenroos, L. Parkkonen, R. J. Ilmoniemi, G. L. Romani, and V. Pizzella. "The Impact of Improved MEG–MRI Co-Registration on MEG Connectivity Analysis". *NeuroImage* 197 (2019), pp. 354–367.
- [83] S. S. Dalal, S. Rampp, F. Willomitzer, and S. Ettl. "Consequences of EEG Electrode Position Error on Ultimate Beamformer Source Reconstruction Performance." *Frontiers in Neuroscience* 8 (March 2014), p. 42.
- [84] D. Khosla, M. Don, and B. Kwong. "Spatial Mislocalization of EEG Electrodes - Effects on Accuracy of Dipole Estimation". *Clinical Neurophysiology* 110.2 (1999), pp. 261–271.
- [85] J. S. George, P. S. Jackson, D. M. Ranken, and E. R. Flynn. "Three-Dimensional Volumetric Reconstruction for Neuromagnetic Source Localization". In: *Advances in Biomagnetism*. Ed. by S. J. Williamson, M. Hoke, G. Stroink, and M. Kotani. Boston, MA: Springer US, 1989, pp. 737–740.
- [86] S. J. Williamson and L. Kaufman. "Advances in Neuromagnetic Instrumentation and Studies of Spontaneous Brain Activity". In: *Brain Topography*. Vol. 2. 1-2. 1989, pp. 129–139.
- [87] H. H. Jasper. "The Ten-Twenty Electrode System of the International Federation". *Electroencephalography and Clinical Neurophysiology* 10.2 (1958), pp. 371–375.
- [88] S. Ahlfors and R. J. Ilmoniemi. "Magnetometer Position Indicator for Multichannel MEG". In: *Advances in Biomagnetism*. Springer, 1989, pp. 693–696.
- [89] J. Nenonen, J. Nurminen, D. Kičić, R. Bikmullina, P. Lioumis, V. Jousmäki, S. Taulu, L. Parkkonen, M. Putaala, and S. Kähkönen. "Validation of Head Movement Correction and Spatiotemporal Signal Space Separation in Magnetoencephalography". *Clinical Neurophysiology* 123.11 (2012), pp. 2180–2191.
- [90] C. Whalen, E. L. Maclin, M. Fabiani, and G. Gratton. "Validation of a Method for Coregistering Scalp Recording Locations with 3D Structural MR Images". *Human Brain Mapping* 29.11 (2008), pp. 1288–1301.
- [91] S. Ettl, S. Rampp, S. Fouladi-Movahed, S. S. Dalal, F. Willomitzer, O. Arold, H. Stefan, and G. Häusler. "Improved EEG Source Localization Employing 3D Sensing by "Flying Triangulation"". *Proceedings SPIE 8791, Videometrics, Range Imaging, and Applications XII; and Automated Visual Inspection 2013* 8791.0 (2013), p. 7.
- [92] T. Bardouille, S. V. Krishnamurthy, S. G. Hajra, and R. C. N. Darcy. "Improved Localization Accuracy in Magnetic Source Imaging Using a 3-D Laser Scanner". *IEEE Transactions on Biomedical Engineering* 59.12 (2012), pp. 3491–3497.

- [93] S. V. K. Murthy, M. MacLellan, S. Beyea, and T. Bardouille. “Faster and Improved 3-D Head Digitization in MEG Using Kinect”. *Frontiers in Neuroscience* 8 (OCT 2014), pp. 1–7.
- [94] U. Baysal and G. Şengül. “Single Camera Photogrammetry System for EEG Electrode Identification and Localization”. *Annals of Biomedical Engineering* 38.4 (2010), pp. 1539–1547.
- [95] L. Troebinger, J. D. López, A. Lutti, D. Bradbury, S. Bestmann, and G. Barnes. “High Precision Anatomy for MEG”. *NeuroImage* 86 (2014), pp. 583–591.
- [96] E. Boto et al. “Moving Magnetoencephalography towards Real-World Applications with a Wearable System”. *Nature* 555 (2018), pp. 657–661.
- [97] C. Pfeiffer, L. M. Andersen, D. Lundqvist, F. Schneiderman, and R. Oostenveld. “Localizing On-Scalp MEG Sensors Using an Array of Magnetic Dipole Coils”. *PLOS ONE* 13.5 (2018), e0191111.
- [98] C. Pfeiffer, S. Ruffieux, L. M. Andersen, A. Kalabukhov, D. Winkler, R. Oostenveld, D. Lundqvist, and J. F. Schneiderman. “On-Scalp MEG Sensor Localization Using Magnetic Dipole-like Coils: A Method for Highly Accurate Co-Registration”. *NeuroImage* (2020), p. 116686.
- [99] H. Xia, a. Ben-Amar Baranga, D. Hoffman, and M. V. Romalis. “Magnetoencephalography with an Atomic Magnetometer”. *Applied Physics Letters* 89.21 (2006), p. 211104.
- [100] V. K. Shah and R. T. Wakai. “A Compact, High Performance Atomic Magnetometer for Biomedical Applications”. *Physics in Medicine and Biology* 58.22 (2013), pp. 8153–8161.
- [101] J. Kitching. “Chip-Scale Atomic Devices”. *Applied Physics Reviews* 5.3 (2018), p. 031302.
- [102] J. Iivanainen, M. Stenroos, and L. Parkkonen. “Measuring MEG Closer to the Brain: Performance of on-Scalp Sensor Arrays”. *NeuroImage* 147 (2017), pp. 542–553.
- [103] E. Boto, R. Bowtell, P. Krüger, T. M. Fromhold, P. G. Morris, S. S. Meyer, G. R. Barnes, and M. J. Brookes. “On the Potential of a New Generation of Magnetometers for MEG: A Beamformer Simulation Study”. *PLOS ONE* 11.8 (2016), e0157655.
- [104] D. F. J. Kimball, E. B. Alexandrov, and D. Budker. “General Principles and Characteristics of Optical Magnetometers”. In: *Optical Magnetometry*. Ed. by D. Budker and D. F. Jackson Kimball. Cambridge University Press, 2013, pp. 3–24.

- [105] T. M. Tierney, N. Holmes, S. Mellor, J. D. López, G. Roberts, R. M. Hill, E. Boto, J. Leggett, V. Shah, M. J. Brookes, R. Bowtell, and G. R. Barnes. “Optically Pumped Magnetometers: From Quantum Origins to Multi-Channel Magnetoencephalography”. *NeuroImage* 199 (2019), pp. 598–608.
- [106] J. Iivanainen. “On-Scalp Magnetoencephalography: Theory, Implementation and Measurements”. Doctoral dissertation. Aalto University, 2020.
- [107] S. J. Seltzer. “Developments in Alkali-Metal Atomic Magnetometry”. Doctoral dissertation. Princeton University, 2008.
- [108] W. Happer. “Optical Pumping”. *Reviews of Modern Physics* 44.2 (1972), pp. 169–250.
- [109] W. Happer and H. Tang. “Spin-Exchange Shift and Narrowing of Magnetic Resonance Lines in Optically Pumped Alkali Vapors”. *Physical Review Letters* 31.5 (1973), pp. 273–276.
- [110] W. Happer and A. C. Tam. “Effect of Rapid Spin Exchange on the Magnetic-Resonance Spectrum of Alkali Vapors”. *Physical Review A* 16.4 (1977), pp. 1877–1891.
- [111] J. C. Allred, R. N. Lyman, T. W. Kornack, and M. V. Romalis. “High-Sensitivity Atomic Magnetometer Unaffected by Spin-Exchange Relaxation”. *Physical Review Letters* 89.13 (2002), p. 130801.
- [112] F. Bloch. “Nuclear Induction”. *Physical Review* 70.7-8 (1946), pp. 460–474.
- [113] C. Cohen-Tannoudji, J. Dupont-Roc, S. Haroche, and F. Laloë. “Diverses résonances de croisement de niveaux sur des atomes pompés optiquement en champ nul. I. Théorie”. *Revue de Physique Appliquée* 5.1 (1970), pp. 95–101.
- [114] R. Slocum and B. Marton. “Measurement of Weak Magnetic Fields Using Zero-Field Parametric Resonance in Optically Pumped He⁴”. *IEEE Transactions on Magnetics* 9.3 (1973), pp. 221–226.
- [115] S. J. Seltzer and M. V. Romalis. “Unshielded Three-Axis Vector Operation of a Spin-Exchange-Relaxation-Free Atomic Magnetometer”. *Applied Physics Letters* 85.20 (2004), pp. 4804–4806.
- [116] J. Iivanainen, R. Zetter, M. Grön, K. Hakkarainen, and L. Parkkonen. “On-Scalp MEG System Utilizing an Actively Shielded Array of Optically-Pumped Magnetometers”. *NeuroImage* 194 (2019), pp. 244–258.
- [117] I. M. Savukov and M. V. Romalis. “Effects of Spin-Exchange Collisions in a High-Density Alkali-Metal Vapor in Low Magnetic Fields”. *Physical Review A* 71.2 (2005), p. 023405.

- [118] J. Sheng, S. Wan, Y. Sun, R. Dou, Y. Guo, K. Wei, K. He, J. Qin, and J.-H. Gao. “Magnetoencephalography with a Cs-Based High-Sensitivity Compact Atomic Magnetometer”. *Review of Scientific Instruments* 88.9 (2017), p. 094304.
- [119] S. Morales, M. C. Corsi, W. Fourcault, F. Bertrand, G. Cauffet, C. Gobbo, F. Alcouffe, F. Lenouvel, M. L. Prado, F. Berger, G. Vanzetto, and E. Labyt. “Magnetocardiography Measurements with ^4He Vector Optically Pumped Magnetometers at Room Temperature”. *Physics in Medicine & Biology* 62.18 (2017), pp. 7267–7279.
- [120] E. Labyt, M.-C. Corsi, W. Fourcault, A. Palacios Laloy, F. Bertrand, F. Lenouvel, G. Cauffet, M. Le Prado, F. Berger, and S. Morales. “Magnetoencephalography With Optically Pumped ^4He Magnetometers at Ambient Temperature”. *IEEE Transactions on Medical Imaging* 38.1 (2019), pp. 90–98.
- [121] S. Knappe, O. Alem, D. Sheng, and J. Kitching. “Microfabricated Optically-Pumped Magnetometers for Biomagnetic Applications”. *Journal of Physics: Conference Series* 723 (2016), p. 012055.
- [122] I. K. Kominis, T. W. Kornack, J. C. Allred, and M. V. Romalis. “A Subfemtotesla Multichannel Atomic Magnetometer”. *Nature* 422.6932 (2003), pp. 596–599.
- [123] K. Kim, S. Begus, H. Xia, S. K. Lee, V. Jazbinsek, Z. Trontelj, and M. V. Romalis. “Multi-Channel Atomic Magnetometer for Magnetoencephalography: A Configuration Study”. *NeuroImage* 89 (2014), pp. 143–151.
- [124] A. P. Colombo, T. R. Carter, A. Borna, Y.-Y. Jau, C. N. Johnson, A. L. Dagel, and P. D. D. Schwindt. “Four-Channel Optically Pumped Atomic Magnetometer for Magnetoencephalography”. *Optics Express* 24.14 (2016), pp. 15403–15416.
- [125] M. V. Balabas, T. Karaulanov, M. P. Ledbetter, and D. Budker. “Polarized Alkali-Metal Vapor with Minute-Long Transverse Spin-Relaxation Time”. *Physical Review Letters* 105.7 (2010), p. 070801.
- [126] M. V. Balabas, K. Jensen, W. Wasilewski, H. Krauter, L. S. Madsen, J. H. Müller, T. Fernholz, and E. S. Polzik. “High Quality Anti-Relaxation Coating Material for Alkali Atom Vapor Cells”. *Optics Express* 18.6 (2010), pp. 5825–5830.
- [127] R. Mhaskar, S. Knappe, and J. Kitching. “A Low-Power, High-Sensitivity Micromachined Optical Magnetometer”. *Applied Physics Letters* 101 (2012), p. 241105.
- [128] A. Borna, T. R. Carter, J. D. Goldberg, A. P. Colombo, Y.-Y. Jau, C. Berry, J. McKay, J. Stephen, M. Weisend, and P. D. Schwindt. “A 20-Channel Magnetoencephalography System Based on Optically Pumped Magnetometers”. *Physics in Medicine & Biology* 62.23 (2017), p. 8909.

- [129] T. Karaulanov, I. Savukov, and Y. J. Kim. “Spin-Exchange Relaxation-Free Magnetometer with Nearly Parallel Pump and Probe Beams”. *Measurement Science and Technology* 27.5 (2016), p. 055002.
- [130] C. Johnson and P. D. D. Schwindt. “A Two-Color Pump Probe Atomic Magnetometer for Magnetoencephalography”. *2010 IEEE International Frequency Control Symposium, FCS 2010* (2010), pp. 371–375.
- [131] W. C. Griffith, S. Knappe, and J. Kitching. “Femtotesla Atomic Magnetometry in a Microfabricated Vapor Cell.” *Optics express* 18.26 (2010), pp. 27167–27172.
- [132] T. H. Sander, J. Preusser, R. Mhaskar, J. Kitching, L. Trahms, and S. Knappe. “Magnetoencephalography with a Chip-Scale Atomic Magnetometer”. *Biomedical Optics Express* 3.5 (2012), pp. 981–990.
- [133] C. N. Johnson, P. D. D. Schwindt, and M. Weisend. “Multi-Sensor Magnetoencephalography with Atomic Magnetometers”. *Physics in Medicine & Biology* 58.17 (2013), p. 6065.
- [134] K. Kamada, D. Sato, Y. Ito, H. Natsukawa, K. Okano, N. Mizutani, and T. Kobayashi. “Human Magnetoencephalogram Measurements Using Newly Developed Compact Module of High-Sensitivity Atomic Magnetometer”. *Japanese Journal of Applied Physics* 54.2 (2015), p. 026601.
- [135] O. Alem, A. M. Benison, D. S. Barth, J. Kitching, and S. Knappe. “Magnetoencephalography of Epilepsy with a Microfabricated Atomic Magnetode.” *Journal of Neuroscience* 34.43 (2014), pp. 14324–14327.
- [136] O. Alem, R. Mhaskar, R. Jiménez-Martínez, D. Sheng, J. LeBlanc, L. Trahms, T. Sander, J. Kitching, and S. Knappe. “Magnetic Field Imaging with Microfabricated Optically-Pumped Magnetometers”. *Optics Express* 25.7 (2017), pp. 7849–7858.
- [137] T. M. Tierney et al. “Cognitive Neuroscience Using Wearable Magnetometer Arrays: Non-Invasive Assessment of Language Function.” *NeuroImage* 181 (March 2018), pp. 513–520.
- [138] J. Osborne, J. Orton, O. Alem, and V. Shah. “Fully Integrated, Standalone Zero Field Optically Pumped Magnetometer for Biomagnetism”. In: *Steep Dispersion Engineering and Opto-Atomic Precision Metrology XI*. Vol. 10548. 2018, pp. 89–95.
- [139] R. M. Hill et al. “A Tool for Functional Brain Imaging with Lifespan Compliance”. *Nature Communications* 10.1 (1 2019), pp. 1–11.
- [140] N. Holmes, J. Leggett, E. Boto, G. Roberts, R. M. Hill, T. M. Tierney, V. Shah, G. R. Barnes, M. J. Brookes, and R. Bowtell. “A Bi-Planar Coil System for Nulling Background Magnetic Fields in Scalp Mounted Magnetoencephalography”. *NeuroImage* 181 (2018), pp. 760–774.

- [141] E. Boto et al. “A New Generation of Magnetoencephalography: Room Temperature Measurements Using Optically-Pumped Magnetometers”. *NeuroImage* 149 (2017), pp. 404–414.
- [142] G. Roberts et al. “Towards OPM-MEG in a Virtual Reality Environment”. *NeuroImage* 199 (2019), pp. 408–417.
- [143] R. M. Hill et al. “Multi-Channel Whole-Head OPM-MEG: Helmet Design and a Comparison with a Conventional System”. *NeuroImage* 219 (2020), p. 116995.
- [144] G. N. Peeren. “Stream Function Approach for Determining Optimal Surface Currents”. Doctoral dissertation. Eindhoven University of Technology, 2003.
- [145] K. C. J. Zevenhoven, H. Dong, R. J. Ilmoniemi, and J. Clarke. “Dynamical Cancellation of Pulse-Induced Transients in a Metallic Shielded Room for Ultra-Low-Field Magnetic Resonance Imaging”. *Applied Physics Letters* 106 (2015), p. 034101.
- [146] B. J. Roth. “Thermal Fluctuations of the Magnetic Field over a Thin Conducting Plate”. *Journal of Applied Physics* 83.2 (1998), pp. 635–638.
- [147] H. J. Sandin, P. L. Volegov, M. A. Espy, A. N. Matlashov, I. M. Savukov, and L. J. Schultz. “Noise Modeling From Conductive Shields Using Kirchhoff Equations”. *IEEE Transactions on Applied Superconductivity* 21.3 (2011), pp. 489–492.
- [148] J. Iivanainen, A. J. Mäkinen, R. Zetter, K. C. J. Zevenhoven, R. J. Ilmoniemi, and L. Parkkonen. “A General Approach for Computing Thermal Magnetic Noise Arising from Thin Conducting Objects”. *arXiv* (2020), p. 2007.08963.
- [149] C. A. Mendonça and J. B. C. Silva. “The Equivalent Data Concept Applied to the Interpolation of Potential Field Data”. *Geophysics* 59.5 (1994), pp. 722–732.
- [150] R. J. Blakely. *Potential Theory in Gravity and Magnetic Applications*. Cambridge University Press, 1996. 468 pp.
- [151] S. Taulu and M. Kajola. “Presentation of Electromagnetic Multichannel Data: The Signal Space Separation Method”. *Journal of Applied Physics* 97 (2005), p. 124905.
- [152] R. Turner. “A Target Field Approach to Optimal Coil Design”. *Journal of Physics D: Applied Physics* 19.8 (1986), pp. L147–L151.
- [153] P. Merkel. “Solution of Stellarator Boundary Value Problems with External Currents”. *Nuclear Fusion* 27.5 (1987), pp. 867–871.
- [154] S. Crozier, S. Dodd, K. Luescher, J. Field, and D. M. Doddrell. “The Design of Biplanar, Shielded, Minimum Energy, or Minimum Power Pulsed B0 Coils”. *Magma: Magnetic Resonance Materials in Physics, Biology, and Medicine* 3.1 (1995), pp. 49–55.

- [155] H. Liu and L. S. Petropoulos. “Spherical Gradient Coil for Ultrafast Imaging”. *Journal of Applied Physics* 81.8 (1997), pp. 3853–3855.
- [156] M. Drevlak. “Automated Optimization of Stellarator Coils”. *Fusion Technology* 33.2 (1998), pp. 106–117.
- [157] L. Forbes and S. Crozier. “Novel Target-Field Method for Designing Shielded Biplanar Shim and Gradient Coils”. *IEEE Transactions on Magnetism* 40.4 (2004), pp. 1929–1938.
- [158] S. Pissanetzky. “Minimum Energy MRI Gradient Coils of General Geometry”. *Measurement Science and Technology* 3.7 (1992), pp. 667–673.
- [159] R. A. Lemdiasov and R. Ludwig. “A Stream Function Method for Gradient Coil Design”. *Concepts in Magnetic Resonance Part B: Magnetic Resonance Engineering* 26B.1 (2005), pp. 67–80.
- [160] M. Poole. “Improved Equipment and Techniques for Dynamic Shimming in High Field MRI”. Doctoral dissertation. University of Nottingham, 2007.
- [161] C. T. Harris, D. W. Haw, W. B. Handler, and B. A. Chronik. “Shielded Resistive Electromagnets of Arbitrary Surface Geometry Using the Boundary Element Method and a Minimum Energy Constraint”. *Journal of Magnetic Resonance* 234 (2013), pp. 95–100.
- [162] M. Abe, T. Nakayama, S. Okamura, and K. Matsuoka. “A New Technique to Optimize the Coil Winding Path for the Arbitrarily Distributed Magnetic Field and Application to a Helical Confinement System”. *Physics of Plasmas* 10.4 (2003), pp. 1022–1033.
- [163] L. M. Koponen, J. O. Nieminen, T. P. Mutanen, M. Stenroos, and R. J. Ilmoniemi. “Coil Optimisation for Transcranial Magnetic Stimulation in Realistic Head Geometry”. *Brain Stimulation* 10.4 (2017), pp. 795–805.
- [164] C. Cobos Sánchez, F. J. Garcia-Pacheco, J. M. G. Rodriguez, and J. R. Hill. “An Inverse Boundary Element Method Computational Framework for Designing Optimal TMS Coils”. *Engineering Analysis with Boundary Elements* 88 (2018), pp. 156–169.
- [165] G. Bringout, K. Grafe, and T. M. Buzug. “Performance of Shielded Electromagnet-Evaluation Under Low-Frequency Excitation”. *IEEE Transactions on Magnetism* 51.2 (2015), pp. 1–4.
- [166] A. J. Mäkinen, R. Zetter, J. Iivanainen, K. C. J. Zevenhoven, L. Parkkonen, and R. J. Ilmoniemi. “Magnetic-Field Modeling with Surface Currents. Part I. Physical and Computational Principles of Bfieldtools”. *Journal of Applied Physics* 128 (2020), p. 063906.
- [167] A. Reusken. “Stream Function Formulation of Surface Stokes Equations”. *IMA Journal of Numerical Analysis* 40 (2018), pp. 109–139.

- [168] B. Levy. “Laplace-Beltrami Eigenfunctions Towards an Algorithm That “Understands” Geometry”. In: *IEEE International Conference on Shape Modeling and Applications 2006 (SMI'06)*. 2006.
- [169] M. Reuter, S. Biasotti, D. Giorgi, G. Patanè, and M. Spagnuolo. “Discrete Laplace–Beltrami Operators for Shape Analysis and Segmentation”. *Computers & Graphics*. IEEE International Conference on Shape Modelling and Applications 2009 33.3 (2009), pp. 381–390.
- [170] M. S. Poole and N. Jon Shah. “Convex Optimisation of Gradient and Shim Coil Winding Patterns”. *Journal of Magnetic Resonance* 244 (2014), pp. 36–45.
- [171] S. Diamond and S. Boyd. “CVXPY: A Python-Embedded Modeling Language for Convex Optimization”. *Journal of Machine Learning Research* 17 (2016), pp. 1–5.
- [172] A. Agrawal, R. Verschueren, S. Diamond, and S. Boyd. “A Rewriting System for Convex Optimization Problems”. *Journal of Control and Decision* 5.1 (2018), pp. 42–60.
- [173] S. S. Hidalgo-Tobon. “Theory of Gradient Coil Design Methods for Magnetic Resonance Imaging”. *Concepts in Magnetic Resonance Part A* 36A.4 (2010), pp. 223–242.
- [174] M. Poole, P. Weiss, H. S. Lopez, M. Ng, and S. Crozier. “Minimax Current Density Coil Design”. *Journal of Physics D: Applied Physics* 43.9 (2010), p. 095001.
- [175] M. S. Poole, P. T. While, H. S. Lopez, and S. Crozier. “Minimax Current Density Gradient Coils: Analysis of Coil Performance and Heating”. *Magnetic Resonance in Medicine* 68.2 (2012), pp. 639–648.
- [176] K. Kratt, V. Badilita, T. Burger, J. G. Korvink, and U. Wallrabe. “A Fully MEMS-Compatible Process for 3D High Aspect Ratio Micro Coils Obtained with an Automatic Wire Bonder”. *Journal of Micromechanics and Microengineering* 20.1 (2010), p. 015021.
- [177] D. Sheng, A. R. Perry, S. P. Krzyzewski, S. Geller, J. Kitching, and S. Knappe. “A Microfabricated Optically-Pumped Magnetic Gradiometer”. *Applied Physics Letters* 110.3 (2017), p. 031106.
- [178] V. H. Souza. “Development of Instrumentation for Neuronavigation and Transcranial Magnetic Stimulation”. Doctoral dissertation. Universidade de São Paulo, 2018.
- [179] M. Poole, R. Bowtell, D. Green, S. Pittard, A. Lucas, R. Hawkes, and A. Carpenter. “Split Gradient Coils for Simultaneous PET-MRI”. *Magnetic Resonance in Medicine* 62.5 (2009), pp. 1106–1111.

- [180] M. Limes, E. Foley, T. Kornack, S. Caliga, S. McBride, A. Braun, W. Lee, V. Lucivero, and M. Romalis. “Portable Magnetometry for Detection of Biomagnetism in Ambient Environments”. *Physical Review Applied* 14.1 (2020), p. 011002.
- [181] A. R. Perry, M. D. Bulatowicz, M. Larsen, T. G. Walker, and R. Wyllie. “An All-Optical Atomic Gradiometer with Sub-20 fT/Cm/ $\sqrt{\text{Hz}}$ Sensitivity in a 22 μT Earth-Scale Magnetic Field”. *arXiv* (2020), p. 2008.13234.
- [182] D. Sheng, S. Li, N. Dural, and M. V. Romalis. “Subfemtotesla Scalar Atomic Magnetometry Using Multipass Cells”. *Physical Review Letters* 110.16 (2013), pp. 1–5.
- [183] S. Li, P. Vachaspati, D. Sheng, N. Dural, and M. V. Romalis. “Optical Rotation in Excess of 100 Rad Generated by Rb Vapor in a Multipass Cell”. *Physical Review A* 84.6 (2011), p. 061403.
- [184] R. Zhang, R. Mhaskar, K. Smith, and M. Prouty. “Portable Intrinsic Gradiometer for Ultra-Sensitive Detection of Magnetic Gradient in Unshielded Environment”. *Applied Physics Letters* 116.14 (2020), p. 143501.
- [185] R. Hari, K. Kaila, T. Katila, T. Tuomisto, and T. Varpula. “Interstimulus Interval Dependence of the Auditory Vertex Response and Its Magnetic Counterpart: Implications for Their Neural Generation”. *Electroencephalography and Clinical Neurophysiology* 54.5 (1982), pp. 561–569.
- [186] H.-L. Halme and L. Parkkonen. “Across-Subject Offline Decoding of Motor Imagery from MEG and EEG”. *Scientific Reports* 8.1 (2018), p. 10087.
- [187] I. Zubarev, R. Zetter, H.-L. Halme, and L. Parkkonen. “Adaptive Neural Network Classifier for Decoding MEG Signals”. *NeuroImage* 197 (2019), pp. 425–434.
- [188] N. Holmes, T. M. Tierney, J. Leggett, E. Boto, S. Mellor, G. Roberts, R. M. Hill, V. Shah, G. R. Barnes, M. J. Brookes, and R. Bowtell. “Balanced, Bi-Planar Magnetic Field and Field Gradient Coils for Field Compensation in Wearable Magnetoencephalography”. *Scientific Reports* 9.1 (1 2019), p. 14196.
- [189] N. V. Nardelli, S. P. Krzyzewski, and S. A. Knappe. “Reducing Crosstalk in Optically-Pumped Magnetometer Arrays”. *Physics in Medicine & Biology* 64.21 (2019), 21NT03.
- [190] J. Wang, X. Song, Y. Le, W. Wu, B. Zhou, and X. Ning. “Design of Self-Shielded Uniform Magnetic Field Coil via Modified Pigeon-Inspired Optimization in Miniature Atomic Sensors”. *IEEE Sensors Journal* (2020).

9 789526 402130



ISBN 978-952-64-0213-0 (printed)

ISBN 978-952-64-0214-7 (pdf)

ISSN 1799-4934 (printed)

ISSN 1799-4942 (pdf)

Aalto University

School of Science

Department of Neuroscience and Biomedical Engineering

www.aalto.fi

**BUSINESS +
ECONOMY**

**ART +
DESIGN +
ARCHITECTURE**

**SCIENCE +
TECHNOLOGY**

CROSSOVER

**DOCTORAL
DISSERTATIONS**